Investigating the Gas Sorption Mechanism in an rht-Metal-Organic Framework Through Computational Studies

13 AUTHORS, INCLUDING:

Tony Pham
University of South Florida
35 PUBLICATIONS **649** CITATIONS

SEE PROFILE

Youssef Belmabkhout
King Abdullah University of Science and Techn…
58 PUBLICATIONS **2,353** CITATIONS

SEE PROFILE

Brian Space
University of South Florida
91 PUBLICATIONS **1,877** CITATIONS

SEE PROFILE

Investigating the Gas Sorption Mechanism in an *rht*-Metal−Organic Framework through Computational Studies

Tony Pham,[†,‡] Katherine A. Forrest,[†,‡] Juergen Eckert,[†] Peter A. Georgiev,[§,‖] Ashley Mullen,[†] Ryan Luebke,[⊥] Amy J. Cairns,[⊥] Youssef Belmabkhout,[⊥] Jarrod F. Eubank,[†] Keith McLaughlin,[†] Wiebke Lohstroh,[#] Mohamed Eddaoudi,[†,⊥] and Brian Space*,[†]

[†]Department of Chemistry, University of South Florida, 4202 East Fowler Avenue, CHE205, Tampa, Florida 33620-5250, United States

[§]Department of Structural Chemistry, University of Milan, 21 Via G. Venezian, I-20133 Milan, Italy

[‖]Faculty of Chemistry and Pharmacy, University of Sofia, 1 James Bourchier Blvd., Sofia 1164, Bulgaria

[⊥]Advanced Membranes and Porous Materials Center, Division of Physical Sciences and Engineering 4700 King Abdullah University of Science and Technology (KAUST) Thuwal 23955-6900, Kingdom of Saudi Arabia

[#]Heinz Maier-Leibnitz Zentrum (MLZ), Technische Universität München, Lichtenbergstraße 1, D-85748 Garching, Germany

S *Supporting Information*

ABSTRACT: Grand canonical Monte Carlo (GCMC) simulations were performed to investigate CO_2 and H_2 sorption in an *rht*-metal−organic framework (MOF) that was synthesized with a ligand having a nitrogen-rich trigonal core through trisubstituted triazine groups and amine functional groups. This MOF was synthesized by two different groups, each reporting their own distinct gas sorption measurements and crystal structure. Electronic structure calculations demonstrated that the small differences in the atomic positions between each group's crystal structure resulted in different electrostatic parameters about the Cu^{2+} ions for the respective unit cells. Simulations of CO_2 sorption were performed with and without many-body polarization effects and using our recently developed CO_2 potentials, in addition to a well-known bulk CO_2 model, in both crystallographic unit cells. Simulated CO_2 sorption isotherms and calculated isosteric heats of adsorption, Q_{st}, values were in excellent agreement with the results reported previously by Eddaoudi et al. for both structures using the polarizable CO_2 potential. For both crystal structures, the initial site for CO_2 sorption were the Cu^{2+} ions that had the higher positive charge in the unit cell, although the identity of this electropositive Cu^{2+} ion was different in each case. Simulations of H_2 sorption were performed with three different hydrogen potentials of increasing anisotropy in both crystal structures and the results, especially with the highest fidelity model, agreed well with Eddaoudi et al.'s experimental data. The preferred site of H_2 sorption at low loading was between two Cu^{2+} ions of neighboring paddlewheels. The calculation of the normalized hydrogen dipole distribution for the polarizable model in both crystal structures aided in the identification of four distinct sorption sites in the MOF, which is consistent to what was observed in the experimental inelastic neutron scattering (INS) spectra. Lastly, while the experimental results for the two groups are quantitatively different, the sorption mechanisms (for both crystal structures and sorbates) are broadly similar and not inconsistent with either set of experimental data; the theoretical sorption isotherms themselves resemble those by Eddaoudi et al.
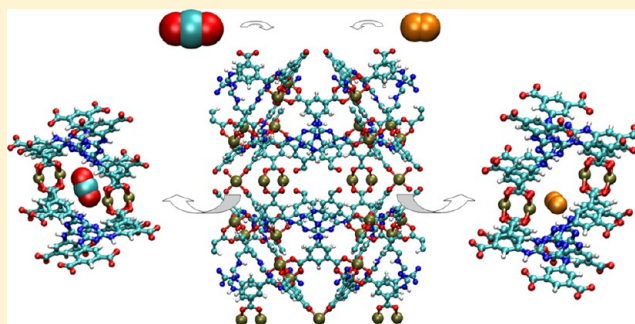
I. INTRODUCTION

Carbon dioxide is the most abundant greenhouse gas that is emitted from the combustion of carbonaceous fuels (e.g., coal, oil, natural gas). Given the abundance of fossil fuel-based energy currently in use, which is roughly 85% of global energy production,[1,2] an about 43% increase in atmospheric CO_2 concentrations over preindustrial levels was observed within the past decade.[3] Indeed, there is a significant amount of CO_2 in the atmosphere and it is contributing greatly to the global warming problem. As the discontinuation of fossil fuel-based energy production is unlikely, capture and sequestration of

greenhouse emissions prior to release into the environment offers an attractive solution. While a number of methods for CO_2 capture currently exist, they tend to either lack long-term viability or have prohibitively expensive implementation requirements.[4,5] Thus, there is a pressing need in this economy to develop methods that can effectively capture CO_2 from postcombustion effluents, such as flue gases.

The use of molecular hydrogen as a fuel source in vehicles has been viewed as a promising strategy to prevent CO_2 emissions.[6] Hydrogen is a clean alternative fuel because the oxidation of hydrogen in an engine releases only water as a byproduct; thus, no greenhouse gases are generated by burning hydrogen. In addition, hydrogen has a relatively high energy capacity, as it releases the most energy per weight of any known fuel. However, an unsolved problem in this energy economy is finding or synthesizing a material that can store a considerable amount of hydrogen at near-ambient temperatures and high pressures and is capable of releasing hydrogen freely due to a mild change in conditions.[7] The ultimate U.S. Department of Energy (DOE) target of 7.5 wt % for the total storage system is a goal that has yet to be reached.[8]

Metal−organic frameworks (MOFs) are a class of porous materials that have been shown to be promising for CO_2 capture/storage and separations[9−11] and H_2 storage.[12−14] MOFs represent a group of crystalline compounds that are composed of rigid organic linkers coordinated to single metal-ions or clusters.[15,16] They can be constructed to have moderate to high surface areas and can be assembled from organic and inorganic moieties with desired chemical functionality.[17] Their modular and tunable character, along with their porous nature, allows them to become suitable materials for CO_2 capture and H_2 storage.[18] Indeed, tremendous progress has been made toward synthesizing materials that can selectively capture CO_2[11] and can store large amounts of hydrogen.[19]

A promising class of MOFs that has been shown to capture/store and separate a considerable amount of CO_2 and H_2 is the *rht*-MOFs.[17,20−36] These MOFs are constructed from a trigonal molecular building block (MBB), which represents a 3-connected node, and a cuboctahedral supermolecular building block (SBB), representing a 24-connected node. It is for this reason that they are also called the (3,24)-connected MOFs. The trigonal MBB is exemplified by a ligand consisting of three coplanar isophthalate moieties and having overall C_3 symmetry. Construction of an *rht*-MOF yields three distinct cages in the framework: cuboctahedron (cub-O_h), truncated tetrahedron (T-T_d), and truncated octahedron (T-O_h).

Recently, an *rht*-MOF was synthesized using 5,5′,5″-(1,3,5-triazine-2,4,6-triyltriimino)tris-isophthalate as the organic linker, giving rise to a MOF that has nitrogen-rich trigonal cores and very narrow pore sizes, especially in comparison to other *rht*-MOFs (Figure 1).[26,29] In the structure of this MOF, each 1,3,5-triazine core is coordinated to secondary amine groups at the 2-, 4-, and 6-positions, which in turn is linked to the 5-position of the isophthalate moieties. The isophthalate groups are coordinated to Cu^{2+} ions to form the well-known copper paddlewheel clusters. This MOF is known as *rht*-MOF-7 and it was synthesized by two different groups: Eddaoudi et al.[29] and Li et al.[26,37] Experimental studies of CO_2 sorption on *rht*-MOF-7 revealed that the MOF is capable of sorbing a significant amount of CO_2. Moreover, it currently has the highest initial isosteric heat of adsorption, Q_{st}, toward CO_2 out of all *rht*-MOFs synthesized thus far. This has been verified by the two groups that performed CO_2 sorption measurements in this MOF. Indeed, the high CO_2 loading in *rht*-MOF-7 can be attributed to the presence of (and synergistic effect between) the open-metal sites, the nitrogen-rich centers through the amine and triazine moieties, and the comparatively small pore size that the MOF exhibits. However, the CO_2 uptakes reported by the two groups were somewhat different as seen in their CO_2 sorption isotherms. For instance, at 298 K and 1.0 atm,
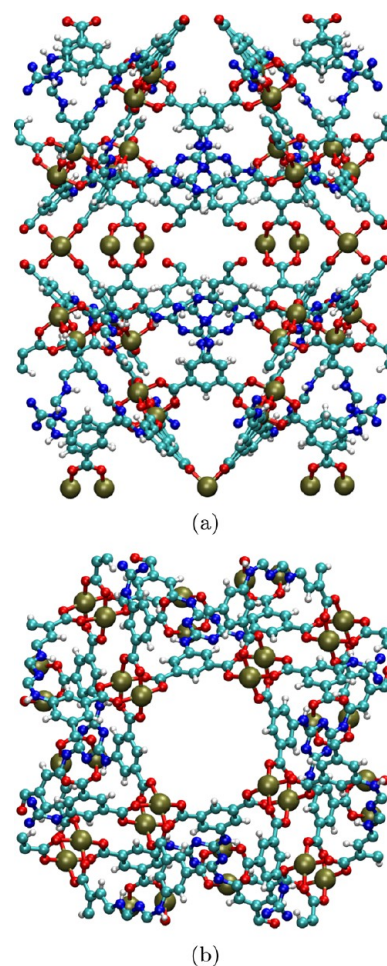

Figure 1. Molecular view of the *rht*-MOF-7 unit cell: (a) side view; (b) top view. Atom colors: C = cyan, H = white, N = blue, O = red, Cu = tan.

Eddaoudi et al. measured a CO_2 uptake of about 3.90 mmol g^{-1}, whereas Li et al. measured about 5.90 mmol g^{-1} under the same conditions.

In addition, experimental H_2 sorption studies on *rht*-MOF-7 by Li et al. showed that the MOF can sorb 2.65 wt % of hydrogen at 77 K and 1.0 atm and has an initial H_2 Q_{st} value of 8.29 kJ mol^{-1}. In this work, we report the experimental hydrogen sorption results that were generated by Eddaoudi et al. On comparison, it was observed that the two experimental groups also have different H_2 sorption results for *rht*-MOF-7. According to the measurements performed by Eddaoudi et al., *rht*-MOF-7 sorbs 2.20 wt % of hydrogen at 77 K and 1.0 atm and has an initial H_2 Q_{st} value of 6.77 kJ mol^{-1}. The experimental inelastic neutron scattering (INS) spectra for hydrogen in *rht*-MOF-7 is also reported herein, which contains a number of transitions that corresponds to specific binding sites in the MOF and is consistent with our simulated sorption.

In this work, we use grand canonical Monte Carlo (GCMC) methods to investigate CO_2 and H_2 sorption in *rht*-MOF-7. GCMC studies can provide atomistically detailed insights into the mechanism of gas sorption while providing direct comparisons to experimental measurements, such as sorption isotherms and associated Q_{st} values.[38−40] In addition, GCMC methods can be used to determine the preferred sorptions sites in a MOF. The simulations performed herein will be compared to the experimental data reported by the two groups.

Furthermore, the two-dimensional quantum rotational levels are calculated for hydrogen about various binding sites in *rht*-MOF-7. The calculated energy levels are directly compared to the transitions that were observed in the INS spectra. Accurate molecular level predictions can be made with confidence if there is excellent agreement between experiment and theory.

Simulations were performed with and without the inclusion of many-body polarization contributions.[41−43] It was shown in previous work on H_2 sorption in the *rht*-MOFs PCN-61[23] and Cu-TPBTM[24] that explicit many-body polarization effects were critical to describe the correct sorption behavior in these MOFs.[40,44] Indeed, it is a significant strength of such polarizable potentials that they can describe interactions with open-metal sites that may be otherwise thought of as essentially quantum mechanical.[45−47] This was performed using accurate and transferable potentials of H_2 that were developed in our group.[48] The same H_2 potentials were used to investigate the hydrogen sorption mechanism in *rht*-MOF-7 through GCMC simulation in this work.

In addition, we have developed analogous CO_2 potentials for use in simulation in condensed phase media. Thus, simulations of CO_2 sorption in *rht*-MOF-7 were performed using these CO_2 potentials: one that includes charge-quadrupole interactions (referred to as CO_2−PHAST), and one that includes charge-quadrupole interactions in addition to explicit induction (referred to as CO_2*−PHAST). This was done in an attempt to better understand the CO_2 sorption mechanism in this MOF. Note, several groups[9,49,50] have used the TraPPE CO_2 model[51,52] in their MOF−CO_2 simulations. Although this model can accurately describe the correct structure in the bulk environment and weakly interacting materials, it does not consistently capture the anisotropy and energetics in systems where induced dipole interactions are important.[53] This CO_2 model was also used in the simulations for comparison given its excellence as a bulk potential.

II. METHODS

A. Simulation Parameters. The force field that was established for *rht*-MOF-7 includes Lennard-Jones repulsion/dispersion parameters (taken from the Universal Force Field[54]), ab initio derived atomic partial charges, and carefully parametrized atomic point polarizabilities as in previous work.[38,40,44,55−59]

The parametrizations and simulations were performed on the crystallographic structure reported by both groups. In this work, the crystal structure reported by Eddaoudi et al. will be referred to as crystal structure A, while the crystal structure reported by Li et al. will be referred to as crystal structure B. Evaluation of the crystal structures reported by both groups via the Cambridge Crystallographic Data Centre (CCDC) revealed that the unit cells were nearly identical with minor differences in the unit cell lengths (Eddaoudi et al.: 26.6700 Å × 26.6700 Å × 38.0416 Å, Li et al.: 26.8604 Å × 26.8604 Å × 37.7538 Å). Although the chemical functionalities (e.g., 1,3,5-triazines, secondary amines, copper paddlewheels) exhibited in both structures are the same, there were minor differences in the crystallographic positions of the atoms, displayed in Figure 2, and this had an effect on the electronic structure calculations for the two unit cells. Nevertheless, the simulated sorption results in both structures were very similar to each another. In addition, it will be shown that simulations in both crystal structures were required to reproduce certain experimental observables.
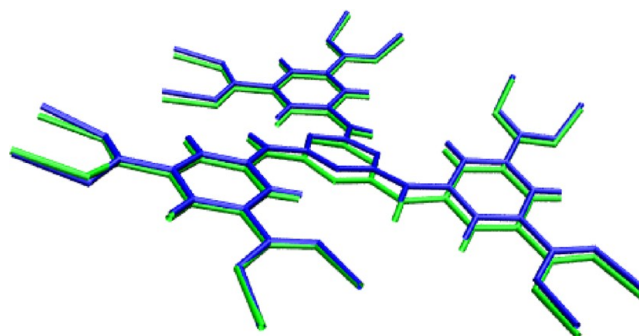

Figure 2. Organic linker of *rht*-MOF-7 showing the relative positions of the different crystal structures used. Crystal structure A = green, crystal structure B = blue.

Note, geometry optimization of the crystal structures in the Vienna ab initio Simulation Package (VASP) code[60−63] was attempted to determine if a shared energy minimum existed between the two structures; however, the calculation was computationally expensive and prohibitive due to the large dimensions of the unit cell lengths. A single-point energy calculation on both structures using VASP showed that both crystal structures may exist. Perhaps an energetically favorable hybrid structure existed between the two structures with characteristics of each. Thus, in this work, the uptakes that were produced within the unit cells by both groups at each state point are reported separately and as averages.

The atomic point partial charges were determined from a series of gas phase fragments that were cut from the *rht*-MOF-7 unit cell. This was done for the crystallographic structures reported by both groups. Note, it was shown that periodic fitting of the entire crystal structure was a more appealing method to calculate partial charges.[55,64,65] However, the size of the unit cell was large enough to make the calculation for the relaxation process computationally expensive and prohibitive. Thus, the partial charges were determined from a fragment-based approach. Examination of the unit cell revealed 21 chemically distinct atoms which produces the entire 960 atom unit cell upon crystallographic symmetry operations (Figure 3). The symmetry of the unit cell was used as a basis for deciding on representational chemical fragments.

It should be noted that in some previously published work on *rht*-MOFs,[17,34,49,66] the two Cu^{2+} ions of the metal paddlewheels have been constrained to equivalence. It is important to emphasize that these two Cu^{2+} ions are in similar but chemically distinct environments as they are located in different regions of the MOF. The ions facing toward the center of the linker, known herein as the Cu1 ions, project into the truncated tetrahedral and truncated octahedral cages, while the ions facing away from the center of the linker, known herein as the Cu2 ions, project into the cuboctahedral cage. While these ions are not identical, as the carboxylate carbon−aromatic carbon bond cannot rotate freely in the MOF, it is common practice to equate these atoms in similar environments. In the case of the Cu^{2+} ions in *rht*-MOFs, however, the difference in relative charge magnitudes have been shown to be significant with the more positive ion acting as the favored sorption site, while the lower charged ion shows little interaction under moderate conditions.[40,44]

The fragments were chosen such that the examined atoms were in a similar chemical environment to the actual framework. Chemical termination of fragments was obtained
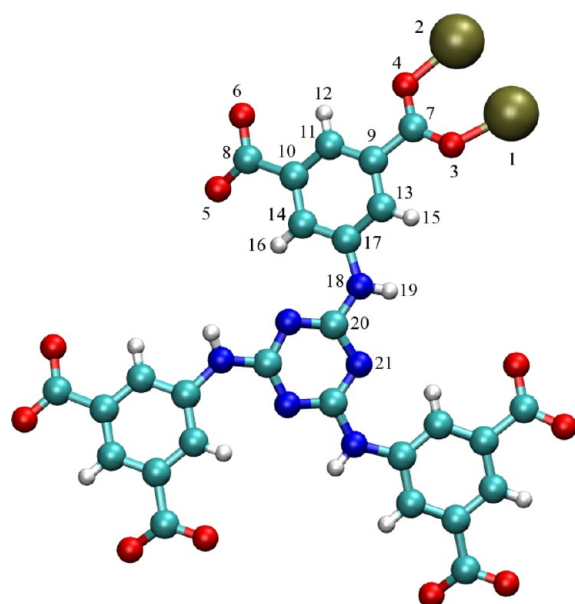
Figure 3. Chemically distinct atoms in *rht*-MOF-7 defining the numbering system corresponding to Table 1. Atom colors: C = cyan, H = white, N = blue, O = red, Cu = tan.

by the addition of hydrogen atoms where appropriate. All light atoms were treated at the 6-31G* level that produces overpolarized charges appropriate for condensed phase simulations.[67] This was done to approximate self-polarization of the condensed phase crystalline environment. The LANL2DZ[68−70] effective core potential basis set was used to represent the many-electron Cu^{2+} ions. The electronic structure calculations were performed using the NWChem ab initio simulation package;[71] this software utilizes the CHELPG method[72,73] to fit the partial charges onto the atomic centers.

It is important to mention that notable discrepancies in the partial charges of the Cu^{2+} ions were observed for a variety of fragments for crystal structure B. In particular, the Cu^{2+} ions, labeled 1 and 2 in Figure 3, alternated charges with atom 1 (Cu1 ion) having the higher charge in a number of fragments and atom 2 (Cu2 ion) having the higher charge in others. In fragments that had two Cu paddlewheels, both cases often occurred simultaneously if like atoms were not constrained to equality. After examining a large number of fragments, two key characteristics were discovered as the basis for selecting viable fragments in crystal structure B: the presence of the triazine group and the orientation of the amine hydrogen atom. It was observed that the presence of the nitrogen atom of the triazine group and the hydrogen atom of the amine group causes the Cu1 ion to increase in charge while the Cu2 ion decreased in charge. Furthermore, the charge of the Cu1 ion increases only if the amine hydrogen atom is oriented toward the Cu1 ion of the paddlewheel. Depending on the location in the *rht*-MOF-7 unit cell, a fragment can be selected such that the amine hydrogen atom is oriented toward the Cu1 ion or away from the ion. It was observed that if the amine hydrogen atom points away from the Cu1 ion, the charge of the Cu1 ion will not increase, even if the triazine group was present. Thus, fragments were selected such that the triazine group was on the same side as the Cu paddlewheel and the amine hydrogen atom was pointing toward the Cu1 ion. Comparison of fragments with these features produced excellent agreement among charges in a number of fragments, with standard deviations of less than 0.1

e^-. The fragments that were selected for *rht*-MOF-7 can be found in the Supporting Information.

Note, the same fragments that were selected for crystal structure B were also selected for crystal structure A. However, in crystal structure A, it was observed through partial charge analysis that the Cu2 ion has the higher charge of the two Cu^{2+} ions. This is true for nearly any fragment that included the copper paddlewheels. Thus, the charges of the Cu^{2+} ions are flipped in crystal structure A relative to crystal structure B. This can be explained by differences in the distances between the two Cu paddlewheels and between the Cu1 ion and the nearest nitrogen atom of the 1,3,5-triazine group in both structures. In crystal structure A, the paddlewheels are farther apart from each other and the Cu1 ion is farther away from the nearest triazine nitrogen atom. Due to these differences, the Cu1 ion cannot experience the complete electron-withdrawing effect from the Cu1 ion of a nearby paddlewheel and the nearest triazine nitrogen atom; thus, it cannot exhibit the higher charge between the two Cu^{2+} ions. Although the disparity in the copper charges between the two unit cells does not significantly alter the higher loading sorption results, it has a dramatic effect on the calculated initial Q_{st} values and the initial sorption sites.

After calculating the partial charges for the atoms on a number of fragments for both structures, the charges were averaged between the fragments. Note, terminal atoms were not included in the averaging. Afterward, the partial charges were adjusted such that the total charge of the framework was equal to zero; these values were assigned as the partial charge for each chemically distinct atom in both unit cells of *rht*-MOF-7. The partial charges that were used in this study are given in Table 1. With the exception of the Cu^{2+} ions, the partial charges for all atoms are very similar between the two unit cells.

The simulations were also performed with many-body polarization interactions that were modeled via the atomic

Table 1. Partial Charges, In Units of Electrons, Used in the Simulations for the Two Crystal Structures of *rht*-MOF-7 Reported by the Two Groups[a]

atom	label	A q (e^-)	B q (e^-)
Cu	1	0.8254	1.3041
Cu	2	1.3110	0.9131
O	3	−0.7176	−0.7216
O	4	−0.7210	−0.7297
O	5	−0.7433	−0.7241
O	6	−0.7154	−0.7331
C	7	0.9130	0.9372
C	8	0.9703	0.9618
C	9	0.0015	−0.0363
C	10	−0.0978	−0.1105
C	11	−0.2095	−0.1810
H	12	0.2114	0.1822
C	13	−0.4080	−0.3725
C	14	−0.2640	−0.2582
H	15	0.2466	0.2220
H	16	0.2318	0.2000
C	17	0.4507	0.4187
N	18	−0.6993	−0.6668
H	19	0.3787	0.3719
C	20	1.0064	0.9665
N	21	−0.9027	−0.8351

[a]Label of atoms corresponds to Figure 3.

point polarizability model. More details of many-body polarization can be found elsewhere[38,40−43,74] and in the Supporting Information. The atomic point polarizabilities for all light atoms used a set of rigorously parametrized empirical values that were shown to be highly transferable.[38,40,43,44,55−58,75−78] These atoms were assigned the exponential polarizabilities (C = 1.28860 Å[3], H = 0.41380 Å[3], O = 0.85200 Å[3], N = 0.97157 Å[3]) and associated damping parameter (λ = 2.1304) provided by the work of van Duijnen et al.[43] An atomic point polarizability value of 2.19630 Å[3] was used to parametrize the Cu^{2+} ions; this parameter was determined in our earlier work in PCN-61.[40]

B. CO_2 Potentials. Two CO_2 potentials that were parametrized using the standard sorbate fitting procedure developed in our group[48] were used for the simulations in this work. The CO_2−PHAST model[53] is a rigid five-site model that includes charge-quadrupole effects via point partial charges that are localized on the atomic centers of the CO_2 molecule. Lennard-Jones repulsion/dispersion parameters are located on the carbon atom and phantom sites extending 1.091 Å from the carbon along the C_∞ axis in each direction. Implicit inclusion of induced dipole effects through adjustments of the extant energetic parameters allows for duplication of experimental results for both bulk CO_2 and sorption in relatively nonpolar MOFs such as MOF-5. In polar MOF environments, however, the increase in induced dipole magnitudes stemming from the interaction between the sorbate molecules and a charged interface results in a failure to reproduce experimental data in simulation, generally underestimating sorption by a significant amount. Note, the nonpolar model can also oversorb the experimental measurements in charged/polar MOFs by a considerable amount as observed in this work at higher densities due to changes in the sorbate packing structure.[55] In these cases, the lack of induced dipole interactions causes an overly favorable orientation between the sorbate molecules and the MOF environment, suggesting that explicit polarization is needed to produce realistic geometries in the MOF environments to decrease the sorption.

CO_2*−PHAST[53] is a version of CO_2−PHAST that includes explicit many-body polarization effects via atomic point polarizabilites localized on the atomic positions. This model reproduces experimental data even in highly charged/polar environments. Further, explicit polarization helps bring the sorption down into line with experimental data in cases where the nonpolar model oversorbs by a large amount. The addition of explicit induction causes alterations in the CO_2*−PHAST repulsion/dispersion and charge-quadrupole parameters relative to those for the CO_2−PHAST model. In addition to changes in the magnitudes of the parameters, the off-site Lennard-Jones parameters for the CO_2*−PHAST model shift to 1.114 Å from the carbon atom.

TraPPE[51,52] is a widely known and used three-site CO_2 model that includes explicit repulsion/dispersion and charge−quadrupole interaction terms on the carbon and oxygen atoms of the molecule. This model was fit to reproduce vapor−liquid equilibria behavior of carbon dioxide and was tested in carbon dioxide/alkane mixtures, producing a highly transferable model for simulation of solutions. Although the TraPPE model was not fit to ab initio dimer interactions, it was found to produce excellent agreement to most of those dimer curves corresponding to interactions that are frequently observed in neat CO_2.[53] However, at heterogeneous solid interfacial systems such as charged/polar MOFs, dimer interactions with negligible contributions to gas/liquid interactions can become significant,

and a model that was not designed to reproduce these interactions cannot be expected to accurately reproduce the experimental data in such systems.

All three models were used in modeling CO_2 sorption in *rht*-MOF-7 to understand the CO_2 sorption mechanism at work. The parameters for the CO_2 models can be found in Table 2.

Table 2. Parameters Used to Characterize the TraPPE, CO_2−PHAST, and CO_2*−PHAST CO_2 Models[a]

model	site	ε (K)	σ (Å)	q (e^-)	α° (Å[3])
TraPPE	C	27.00000	2.80000	0.70000	0.00000
	O	79.00000	3.05000	−0.35000	0.00000
	C	8.52238	3.05549	0.77108	0.00000
CO_2−PHAST	O	0.00000	0.00000	−0.38553	0.00000
	OS	76.76607	2.94473	0.00000	0.00000
	C	19.61757	3.30366	0.77134	1.22810
CO_2*−PHAST	O	0.00000	0.00000	−0.38567	0.73950
	OS	46.47457	2.99429	0.00000	0.00000

[a]C and O corresponds to the carbon and oxygen atoms, respectively. OS refers to the off-site positions.

C. H_2 Potentials. Hydrogen sorption was performed in *rht*-MOF-7 using three different hydrogen potential energy functions of increasing anisotropy. The first model, here designated Buch,[79] is a single site model that includes only van der Waals repulsion/dispersion parameters. The second model, known as BSS,[48] is a five-site model that includes repulsion/dispersion and charge-quadrupole interaction parameters. The partial charges are located on the center-of-mass site and the true atomic locations of the H atoms. The Lennard-Jones parameters are localized on the center-of-mass site and two off-site positions that extend 0.329 Å away from the median site. The third model, called BSSP,[48] is an analogue of the previous model with explicit many-body polarization terms. The center-of-mass site and the atomic sites include the partial charges and atomic point polarizability parameters. The off-site positions in this model are shifted to 0.363 Å from the median site. All three models have been shown to reproduce bulk thermodynamic properties of hydrogen up to liquid densities.[48,79,80] The BSS and BSSP models can both describe the accurate sorption of H_2 in relatively nonpolar MOFs such as MOF-5[81] and in polar MOFs with extremely narrow pore sizes,[55,56] but it is the BSSP model that accurately describes the correct sorption behavior in charged/polar MOFs with high surface areas where induced dipole energetics are critical for sorption of hydrogen onto the open-metal sites.[40,44] The parameters for the three hydrogen potentials can be found in Table 3.

Table 3. Parameters Used to Characterize the Buch, BSS, and BSSP H_2 Models[a]

model	site	ε (K)	σ (Å)	q (e^-)	α° (Å[3])
Buch	COM	34.20000	2.96000	0.0000	0.00000
	COM	8.85160	3.22930	−0.7464	0.00000
BSS	H	0.00000	0.00000	0.3732	0.00000
	OS	4.06590	2.34060	0.0000	0.00000
	COM	12.76532	3.15528	−0.7464	0.69380
BSSP	H	0.00000	0.00000	0.3732	0.00044
	OS	2.16726	2.37031	0.0000	0.00000

[a]COM refers to the center-of-mass (median) site, H corresponds to the true atomic locations, and OS refers to the off-site positions.

III. RESULTS AND DISCUSSION

A. CO$_2$ Sorption. The GCMC-simulated CO$_2$ sorption isotherms for the three CO$_2$ potentials in *rht*-MOF-7 at 298 K are shown in Figure 4a and compared to the two sets of experimental data. More details of the GCMC methods, including a description of how certain thermodynamic properties are calculated can be found in the Supporting Information. The simulated isotherms for the CO$_2$−PHAST and CO$_2$*−PHAST models in both crystal structures were in excellent agreement with Eddaoudi et al.'s experimental data, while the results underestimate Li et al.'s data by a significant amount. The average uptakes that were produced between the simulation in both unit cells are also in outstanding agreement with Eddaoudi et al.'s results. In contrast, simulations using the TraPPE model produced isotherms that are in reasonable agreement, at least at higher loadings, with Li et al.'s experimental data. TraPPE has been shown to often oversorb in heterogeneous environments and to give generally unpredictable results for sorption in MOFs with strong interactions.[53,56,58] In addition, examination of the modeled unit cell for simulations using the TraPPE potential revealed that the majority of CO$_2$ molecules were essentially sorbing to regions that are dominated by van der Waals and electrostatic interactions, specifically, the corners of the truncated tetrahedral cages. Thus, the TraPPE model produces higher CO$_2$ uptake than the other two models at higher pressures because the TraPPE CO$_2$ molecules are simply sorbing to regions where van der Waals and electrostatic interactions dominate. Further, it can been seen that the uptakes produced by the TraPPE model are lower than those for the CO$_2$*−PHAST model at low loading, which indicates that the TraPPE model does not capture sorption onto the open-metal sites and other highly favorable sorption sites as effectively as the polarizable model.

Considering our most reliable CO$_2$*−PHAST model, it can be seen that at 298 K and low pressures, simulations in crystal structure A undersorb both experimental isotherms while simulations in crystal structure B produce uptakes in excess of those reported by Eddaoudi et al., resulting in good agreement with this experimental isotherm for the average value. At higher pressures and/or lower temperatures, the situation reverses with crystal structure A producing higher uptakes. The superiority of crystal structure B as a sorbent under very mild conditions is attributed to the initial sorption site consisting of binding between two Cu1 ions simultaneously, which corresponds to a highly favorable interaction. In crystal structure A, this site is less favorable owing to the higher electron density about the Cu1 ions in this unit cell, which reduces the interaction potential with the CO$_2$ oxygen atoms. As a result, the immediate saturation of this site in the former structure results in higher uptakes than sorption onto a single Cu2 ion, the less favorable primary sorption site in crystal structure A. Under more extreme conditions, loading into secondary sites occurs, for which crystal structure A proves to be the more favorable structure; this results in uptakes in excess of those for crystal structure B.

The 298 K experimental CO$_2$ isotherms reported by Eddaoudi et al. and Li et al. are vastly different, with Li et al. measuring a CO$_2$ uptake of approximately 1.5 times higher for all low-pressure state points. Experimental results also show deviations in CO$_2$ uptakes at other temperatures between the two groups, particularly 288 and 273 K. The simulated CO$_2$
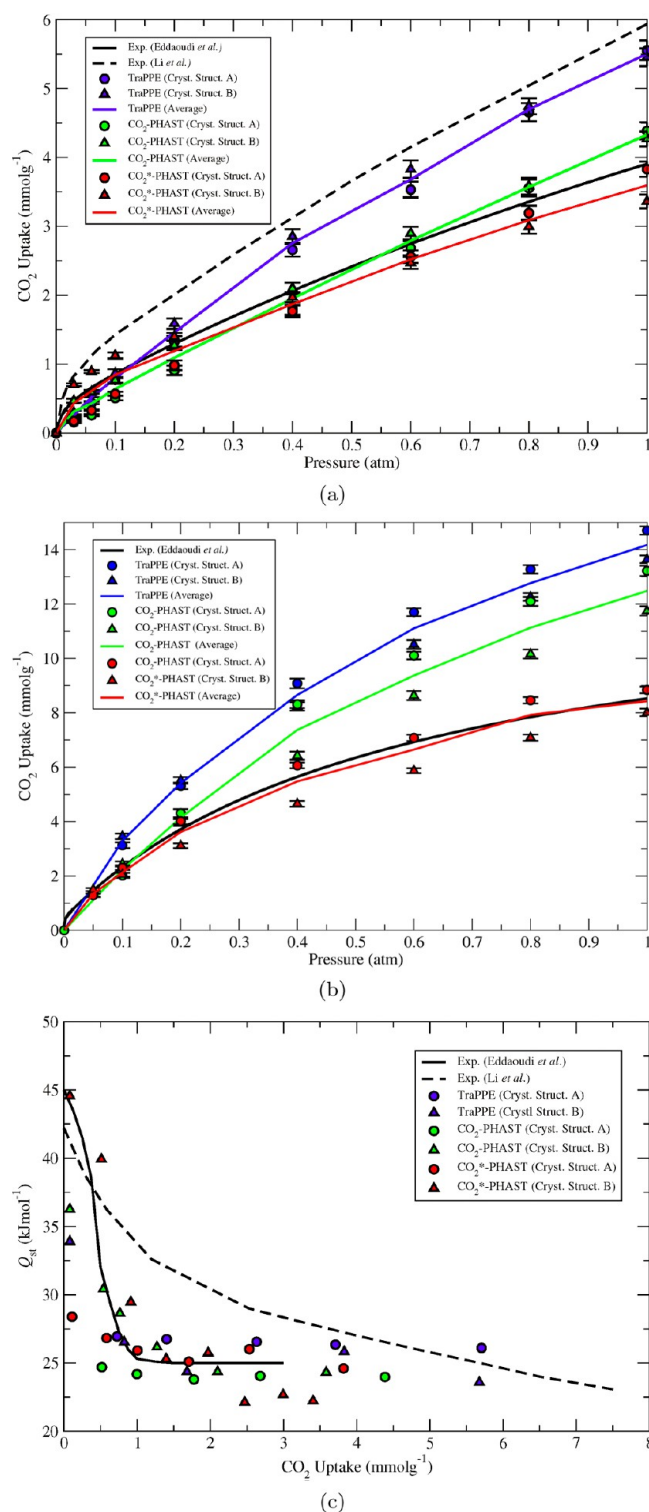

Figure 4. Low pressure (up to 1.0 atm) CO$_2$ sorption isotherms in *rht*-MOF-7 at (a) 298 K and (b) 258 K for experiment (Eddaoudi et al. = solid black, Li et al. = dashed black), TraPPE model (blue), CO$_2$−PHAST model (green), and CO$_2$*−PHAST model (red). (c) Isosteric heats of adsorpion, Q_{st}, in *rht*-MOF-7. The shapes indicate the unit cell in which the simulation was performed in, with circles corresponding to crystal structure A and triangles corresponding to crystal structure B. The average between the two unit cells are represented by the colored solid lines.

sorption isotherms compared to experimental data at other temperatures can be found in the Supporting Information.

Simulations of CO_2 sorption were also performed in *rht*-MOF-7 at these temperatures, and the results agreed well with Eddaoudi et al.'s data for the CO_2^*−PHAST model. Note, the CO_2−PHAST model was observed to oversorb Eddaoudi et al.'s experimental data and producing higher uptakes than the CO_2^*−PHAST model at lower temperatures (e.g., 273 K). This is because the lack of explicit polarization for the CO_2−PHAST model leads to less structured sorbate packing mechanisms at high densities. The inclusion of induced dipole interactions results in distinct sorbate geometries in the MOF structure while decreasing overall sorption. Further, Eddaoudi et al. also reported a CO_2 sorption isotherm at 258 K. The simulated CO_2 isotherms at this temperature agreed well with the corresponding experimental data for only the CO_2^*−PHAST model (Figure 4b). It can be seen that the TraPPE and CO_2−PHAST models oversorb the experimental data by a significant amount due to reasons descibed above for the respective models.

Figure 4c shows the GCMC-calculated Q_{st} values at 298 K for all models compared to the two sets of experimental data. The Q_{st} values produced by the three models in both unit cells are in excellent agreement with Eddaoudi et al.'s experimental data for CO_2 loadings between 0.50 and 4.0 mmol g^{-1}. The high initial Q_{st} value at zero loading corresponds to a strong interaction between the CO_2 molecules and the open-metal sites. This value was reproduced using the CO_2^*−PHAST model for simulation in crystal structure B. Note, this high initial Q_{st} value was only reproduced from the simulation involving explicit polarization in crystal structure B and not crystal structure A. Electronic structure calculations showed that the Cu1 ions (the ions facing toward the center of the linker) had the higher partial positive charge in crystal structure B, whereas the opposite was observed in crystal structure A (see section IIA). This difference in partial charges in the Cu^{2+} ions of the paddlewheels have led to a different initial Q_{st} when simulating in both structures. It was determined from our studies that the higher charge on the Cu1 ion (observed in crystal structure B) is needed for the initial binding of CO_2 molecules between the two Cu1 ions of adjacent paddlewheels; this initial sorption site correlates to the high initial Q_{st} for *rht*-MOF-7. Without the higher static dipole parameters for the Cu1 ion, the ions cannot hold onto the CO_2 molecules very tightly through induction, and this causes the initial Q_{st} to drop. However, as the loading increases, the Q_{st} values are similar for both structures. In addition, it can be seen that the simulations capture the step that is observed in Eddaoudi et al.'s Q_{st} data. The lower Q_{st} value calculated for the CO_2−PHAST and TraPPE models at low loadings compared to Eddaoudi et al.'s data indicates that implicit induction is not enough to completely describe sorption onto the open-metal sites at these loadings due to weaker interactions between the sorbate molecule and the metal. However, as the loading increases and the sites continue to fill, the calculated Q_{st} values for the CO_2−PHAST and TraPPE models matches the values reported by Eddaoudi et al.

Figure 5 shows the difference histogram plot in *rht*-MOF-7 for the CO_2^*−PHAST and TraPPE models at 298 K and 0.20 atm in crystal structure B, where the sites of significant occupancy are shown for one CO_2 potential, but not the other, and vice versa. The three-dimensional histogram reveals notable differences within the sorption sites between the two models at this loading. It can be seen that the majority of sorbate molecules using the CO_2^*−PHAST model are located in the
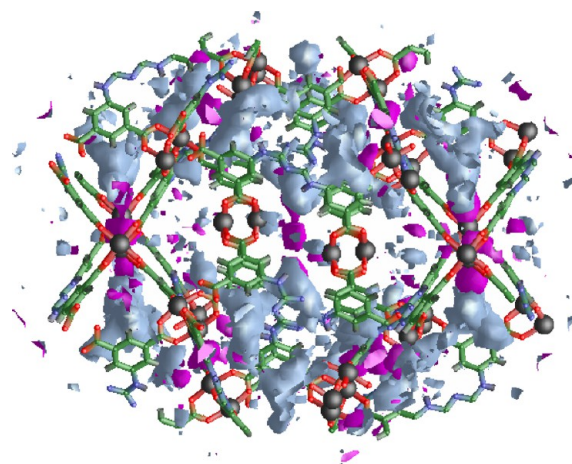

Figure 5. Three-dimensional difference histogram showing the sites of CO_2 sorption for the CO_2^*−PHAST and TraPPE potentials in *rht*-MOF-7 at 298 K and 0.20 atm. The magenta regions indicate occupancy for the CO_2^*−PHAST model, but not for the TraPPE model. The gray regions indicate occupancy for the TraPPE model, but not for the CO_2^*−PHAST model. The results are shown for crystal structure B.

region between two Cu1 ions of neighboring paddlewheels. Specifically, the center-of-mass of the sorbed CO_2 molecules for the CO_2^*−PHAST model are nearly equidistant from the two Cu1 ions. This is a highly favorable site for CO_2 sorption at low loading, and the polarizable model captures this interaction greatly. This site is frequently occupied in crystal structure B relative to crystal structure A because of the higher positive charge on the Cu1 ions in the former.

In contrast, the TraPPE model captures a few CO_2 molecules sorbing in the region of the Cu1 ions at low loading. This indicates that sorption onto the Cu1 ions is less prominent for the TraPPE model compared to the CO_2^*−PHAST model. Moreover, it can be seen in the histogram that the majority of TraPPE CO_2 molecules are sorbed into the corners of the truncated tetrahedral cages. The binding of CO_2 molecules in this area is governed by van der Waals and charge-quadupole interactions. Thus, the TraPPE potential produces higher CO_2 uptakes for simulation in *rht*-MOF-7 because a significant quantity of these molecules are essentially crowding into the corners of the truncated tetrahedral cages across all loadings. On the other hand, the aforementioned region becomes occupied only at higher loadings for the CO_2^*−PHAST models, after the open-metal sites are occupied. Note, a similar difference histogram can be seen for the CO_2^*−PHAST and TraPPE models in crystal structure A, except that the CO_2 molecules are sorbed in the region of the Cu2 ions in this unit cell for the former model.

The radial distribution functions, g(r), of CO_2 carbon atoms at 298 K and 0.20 atm about the Cu1 and Cu2 ions show notable differences between the models as well as the crystal structures (Figure 6). When examining the radial distribution functions about the Cu1 ions, all simulated results have a dominant peak at approximately 3.25 Å from the metal (Figure 6a); this peak correlates to sorption between the two Cu1 ions of adjacent paddlewheels. Indeed, examination of the system's coordinates reveals one CO_2 oxygen atom sorbing onto the Cu1 ion of one paddlewheel and the other oxygen atom sorbing onto said ion of a nearby paddlewheel (Figure 7a). Thus, a favorable interaction can be seen as the CO_2 molecules
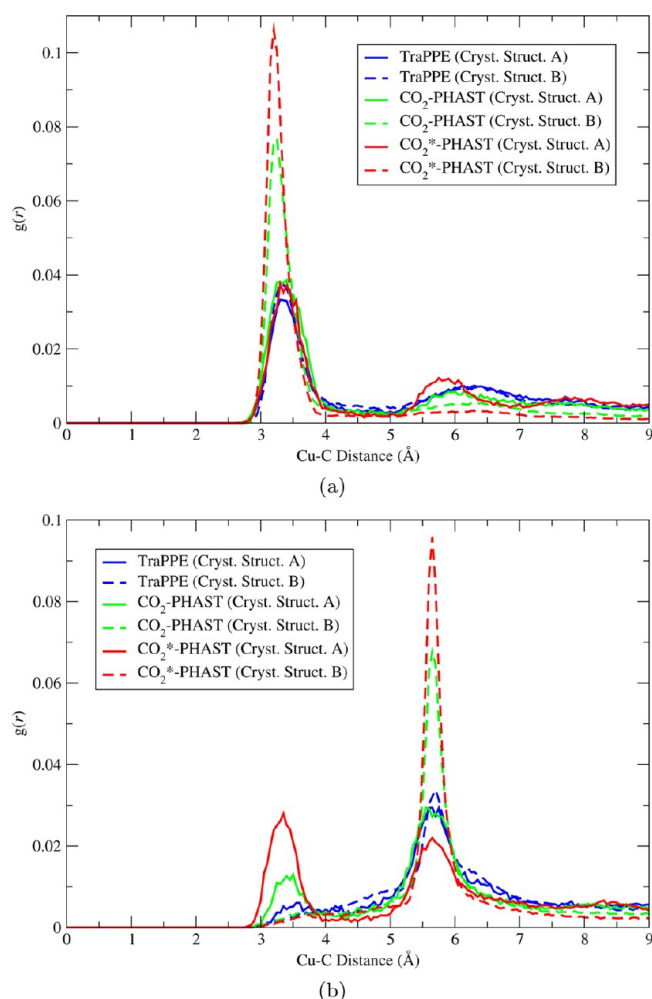
445

dx.doi.org/10.1021/jp409950r | *J. Phys. Chem. C* 2014, 118, 439−456

(a)

(b)

Figure 6. Radial distribution function, g(r), of CO_2 carbon atoms about (a) the Cu1 ions (atom label 1 in Figure 3) and (b) the Cu2 ions (atom label 2 in Figure 3) in *rht*-MOF-7 at 298 K and 0.20 atm for the TraPPE model (blue), CO_2–PHAST model (green), and CO_2*–PHAST model (red). Line type indicate the unit cell in which the simulation was performed in, with solid corresponding to crystal structure A and dashed corresponding to crystal structure B.

(a)

(b)

Figure 7. Molecular illustration of the CO_2*–PHAST CO_2 molecule orientation about (a) the Cu1 ion (atom label 1 in Figure 3) and (b) the Cu2 ion (atom label 2 in Figure 3) in *rht*-MOF-7. Atom colors: C = cyan, H = white, N = blue, O = red, Cu = tan.

locked in between the Cu1 ions of adjacent paddlewheels. This interaction explains why the experimental initial Q_{st} value is so high in this MOF, as the very narrow pore sizes exhibited by *rht*-MOF-7 allows this strong interaction to be possible. Tuning the pore size of a MOF can lead to an optimal interaction between sorbate molecules and the framework.[11]

As shown in Figure 6a, noticeable differences in the magnitude of the 3.25 Å radial distribution peak were observed between the models and the crystal structures. All models in crystal structure A have similar peaks, as does the TraPPE model in crystal structure B. The 3.25 Å radial distribution peak for the CO_2–PHAST and CO_2*–PHAST models in crystal structure B deviate with magnitudes of twice and 2.5 times that of crystal structure A, respectively. It can be observed that sorption between the two Cu1 ions is a favorable sorption site for all models and crystal structures. Higher affinities exist in crystal structure B, which has higher static dipole parameters on the Cu1 ions. Further, these higher charges on the Cu1 ions induce larger dipoles on the CO_2 molecule, which results in a significant enhancement of Cu–CO_2 interactions. A smaller secondary peak is relatively flat for all models but does have
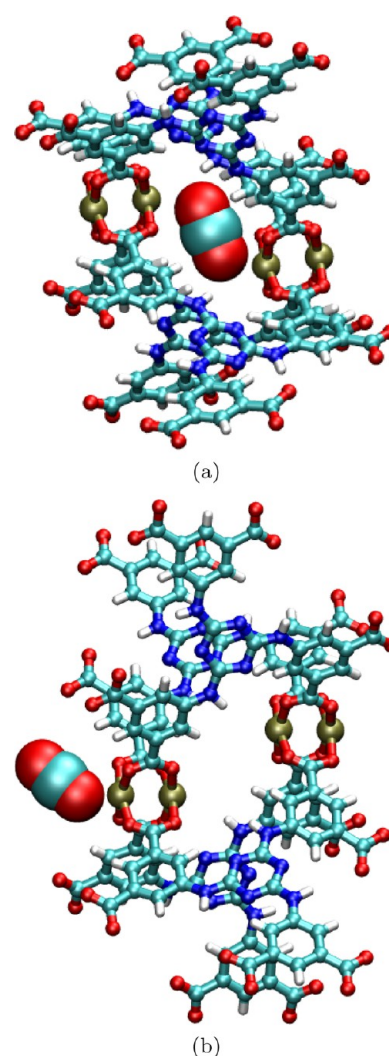
higher occupancy for crystal structure A, with the CO_2*–PHAST model showing a notable shift toward the ion. Note, the CO_2*–PHAST model in crystal structure B is most consistent with the initial Q_{st} value observed experimentally. It is also interesting that the CO_2–PHAST nonpolar model does a reasonable job of capturing this interaction even without explicit polarization.

The radial distribution functions about the Cu2 ions reveal two peaks, with the 5.75 Å radial distribution peak corresponding to sorption onto the Cu1 ions and showing a similar spread of occupancies (Figure 6b). The nearest-neighbor peak at 3.25 Å, however, corresponds to the sorption of CO_2 onto the Cu2 ions (Figure 7b) and is a partial contributor to the secondary peak in the g(r) about the Cu1 ions. Notably, the peak shows negligible populations in crystal structure B but significant occupancies for the CO_2*–PHAST model in crystal structure A. The CO_2–PHAST model generated approximately half of the CO_2*–PHAST result for the 3.25 Å radial distribution peak in crystal structure A, while the TraPPE model yielded results that are only slightly higher than the corresponding results in crystal structure B. It is apparent that the lower charge observed on the Cu2 ion of

crystal structure B is insufficient to motivate sorption onto this site under these conditions, indicating that sorption onto the lower charged Cu1 ion in crystal structure A is facilitated by the interaction of two such metal sites. Additionally, explicit dipole interactions act as a strong contributing force to $Cu-CO_2$ sorption mechanisms.

The aforementioned nearest-neighbor peak distance for sorption onto the Cu^{2+} ions is comparable to the $Cu-CO_2$ distances observed in HKUST-1, a prototypical MOF with copper paddlewheel clusters, which have been determined experimentally via neutron powder diffraction (NPD).[82] The deviation in the magnitudes of the 3.25 Å radial distribution peak between the CO_2 models in crystal structure B can be explained by an increase in sorption onto the open-metal sites with the inclusion of explicit induction for the CO_2*-PHAST model. It can be inferred that, while sorption onto this site is not motivated solely by induced dipole effects, the absence of this interaction causes a more shallow energy minimum. Notably, at very low pressures where the open-metal sites are not fully saturated, the CO_2-PHAST and TraPPE models undersorbs Eddaoudi et al.'s experimental isotherm, a result that is consistent with weaker attraction to the initial loading sites.

Figure 8 shows the normalized distribution of induced dipoles for the CO_2*-PHAST model in both reported crystal
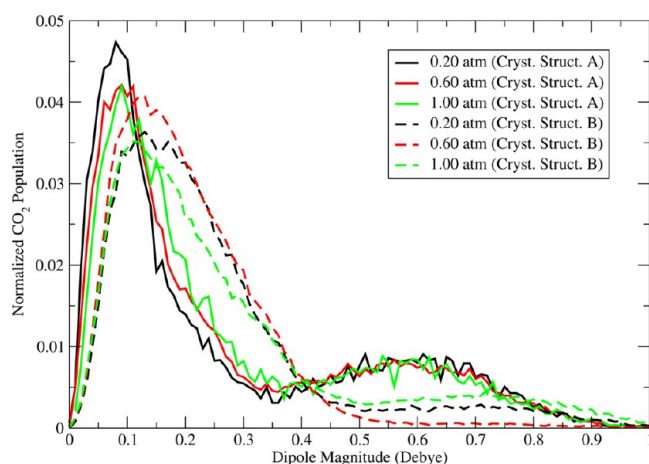

Figure 8. Normalized CO_2 dipole distribution at 298 K and various pressures for the CO_2*-PHAST model in *rht*-MOF-7. Line types indicate the unit cell in which the simulation was performed, with solid corresponding to crystal structure A and dashed corresponding to crystal structure B.

structures for *rht*-MOF-7 at 298 K and various pressures. Simulations in both unit cells show similar bimodal distributions, though notable shifts in the magnitudes were observed. The high dipole peak, ranging from 0.35 to 1.0 D for crystal structure A (Figure 9a) and 0.45 to 1.0 D for crystal structure B (Figure 10a), corresponds to sorption directly onto the open-metal sites. In both cases, the CO_2 molecules are attracted to the Cu^{2+} ion with the lower electron density, as indicated by relative partial charge magnitudes (Cu2 in crystal structure A, Cu1 in crystal structure B). The higher dipole magnitudes for crystal structure B are consistent with sorption onto the Cu1 ion sites since this site corresponds to the high initial CO_2 Q_{st} value in this MOF. This is a consequence of the tendency of the sorbate molecule to bind onto two neighboring Cu1 ions simultaneously, resulting in a stronger interaction
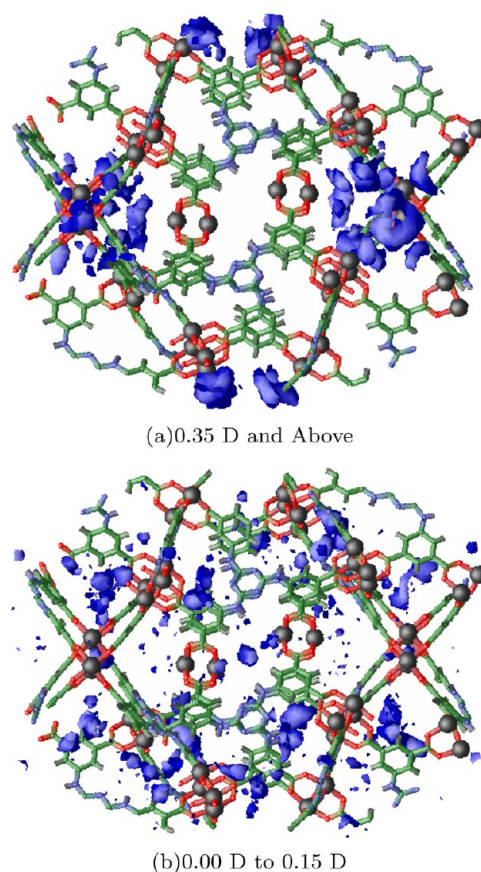

(a)0.35 D and Above

(b)0.00 D to 0.15 D

Figure 9. 3-D histograms of CO_2 sorption for the CO_2*-PHAST model in *rht*-MOF-7 at 298 K and 0.20 atm showing the regions of occupancy (blue) as a function of induced dipole magnitude for crystal structure A: (a) 0.35 D and above; (b) 0.00 to 0.15 D. Atom colors: C = green, H = white, N = blue, O = red, Cu = black.

than that observed for sorption onto a single Cu2 ion as observed in crystal structure A.

While crystal structure A exhibits a moderate amount of sorbate interaction with the Cu1 ions, the less optimal Cu−Cu distance as well as the higher electron density on the Cu1 ions causes said ions to induce dipoles of lesser magnitude on the CO_2 molecules, which do not contribute to the peak ranging from 0.35 to 1.0 D. Rather, this peak for crystal structure A corresponds to the loading of CO_2 molecules onto the Cu2 ions, which is a site that is not observed in crystal structure B due to the lower partial charge on this ion. Because a single Cu2 ion can coordinate to a given CO_2 molecule, the number of available sorption sites for the Cu2 ions is double that of the Cu1 ion, resulting in the greater occupancy observed for crystal structure A. The low dipole magnitude peaks for both unit cells correspond to sorption into the corners of the truncated tetrahedral and truncated octahedral cages as well as sorption onto the Cu1 ions for crystal structure A and secondary sorption in that region for both structures (Figures 9b and 10b).

B. H₂ Sorption. H_2 sorption in *rht*-MOF-7 was simulated at 77 and 87 K using GCMC methods to compare with experimental measurements and perhaps shed light on the variations observed between the different measurements. The low pressure (up to 1.0 atm) H_2 sorption isotherms for all three hydrogen potentials compared to Eddaoudi et al.'s and Li et al.'s experimental data at 77 K are shown in Figure 11a. The
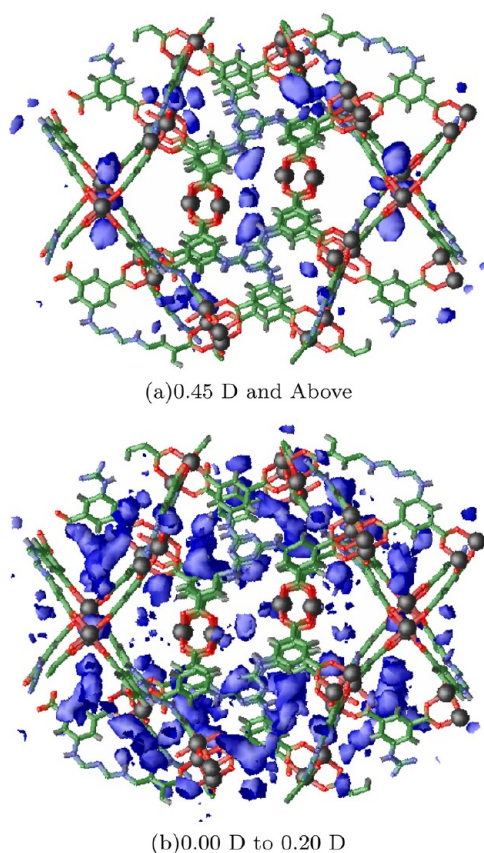
(a)0.45 D and Above

(b)0.00 D to 0.20 D

Figure 10. 3-D histograms of CO_2 sorption for the CO_2*−PHAST model in *rht*-MOF-7 at 298 K and 0.20 atm showing the regions of occupancy (blue) as a function of induced dipole magnitude for crystal structure B: (a) 0.45 D and above; (b) 0.00 to 0.35 D. Atom colors: C = green, H = white, N = blue, O = red, Cu = black.

Buch model, a control potential with only Lennard-Jones interactions, undersorbs Eddaoudi et al.'s experimental data in both unit cells, especially at low pressures, suggesting that van der Waals interactions do not describe sorption at initial loading in polar MOFs accurately. However, it can be seen that the Buch model isotherms come closely in line with Eddaoudi et al.'s data at 1.0 atm. The Buch model isotherms in both unit cells are very similar to each other, and this was to be expected since both unit cells were treated with UFF Lennard-Jones parameters for all atoms to describe repulsion/dispersion interactions. Note, by ambient pressures the material is acting primarily as a container for H_2.

The BSS and BSSP model isotherms in both unit cells are in outstanding agreement with Eddaoudi et al.'s experimental data for pressures up to 0.30 atm. At pressures beyond 0.30 atm, the simulated isotherms trend slightly higher than Eddaoudi et al.'s data. As a result, the simulated uptakes lie between the two sets of experimental data at 1.0 atm. The experimental hydrogen uptake at 77 K and 1.0 atm in *rht*-MOF-7 as measured by Eddaoudi et al. and Li et al. are about 11.14 and 13.50 mmol g^{-1}, respectively. The simulated uptakes for the BSS and BSSP models in both crystal structures under the same conditions range from 12.08 to 12.33 mmol g^{-1}. Hence, the simulated isotherms are still closer to Eddaoudi et al.'s results. It can be seen that polarization contributes less proportionally to the sorption for hydrogen in *rht*-MOF-7; this can be explained by the small pore size exhibited by the MOF, as smaller pores cause van der Waals interactions to dominate for gas sorption.
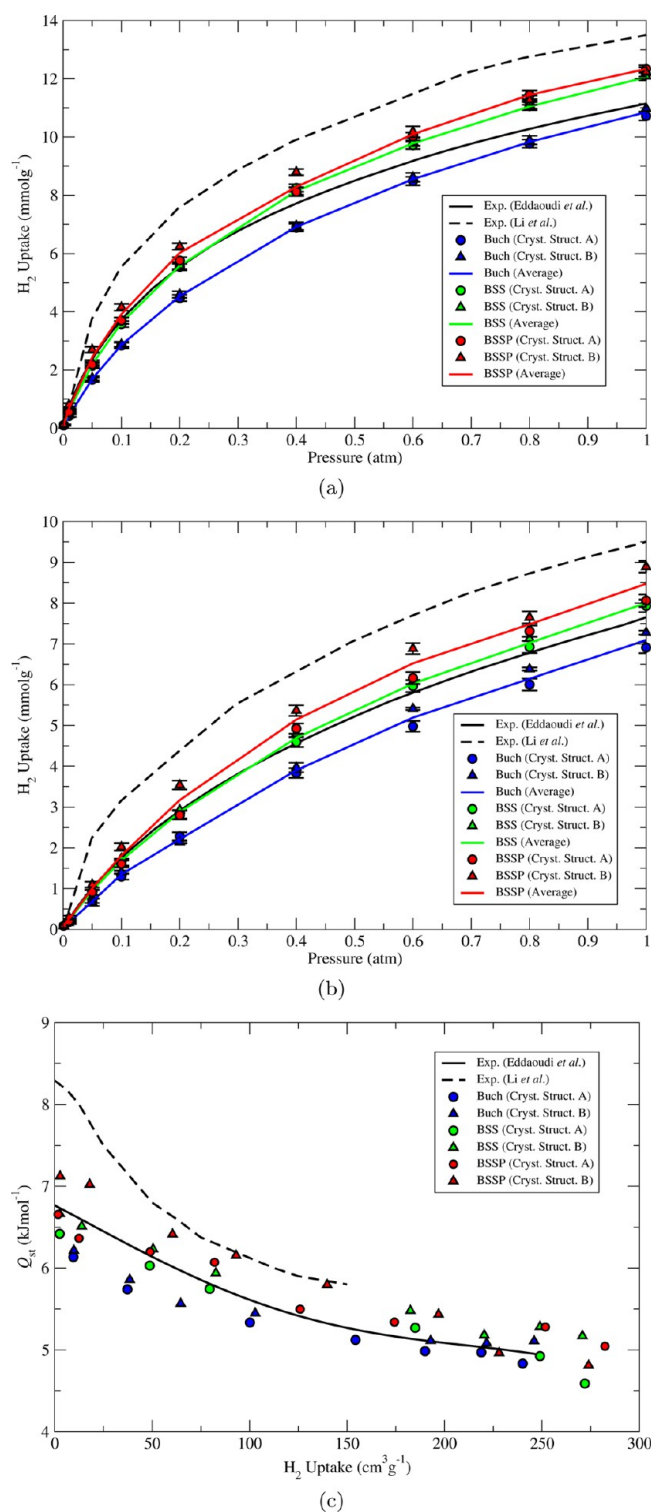

(a)

(b)

(c)

Figure 11. Low-pressure (up to 1.0 atm) absolute hydrogen sorption isotherms in *rht*-MOF-7 at (a) 77 K and (b) 87 K for experiment (Eddaoudi et al. = solid black, Li et al. = dashed black), Buch model (blue), BSS model (green), and BSSP model (red). (b) Isosteric heats of adsorption, Q_{st}, for hydrogen in *rht*-MOF-7. The shapes indicate the unit cell in which the simulation was performed in, with circles corresponding to crystal structure A and triangles corresponding to crystal structure B. The average between the two unit cells are represented by the colored solid lines.

Note, the hydrogen sorption results at 87 K show analogous trends for the simulated sorption isotherms for the three

hydrogen potentials compared to the two sets of experimental data in both crystal structures (Figure 11b). Here, though, the data by Li et al. seems significantly higher than any of the theoretical models that surround the data by Eddaoudi et al.

The isotherms for the BSS model, a potential including charge–quadrupole interactions and some implicit polarization, in both unit cells are nearly identical. This implies that electrostatic interactions cannot distinguish between the hydrogen sorption characteristics of both crystal structures of *rht*-MOF-7. The BSSP model uptakes in crystal structure B are slightly higher than those produced in crystal structure A at 77 K and low pressures, which can be explained by more hydrogen molecules sorbing onto the Cu1 ions of the paddlewheels in the former. Crystal structure B consists of the higher partial charge on the Cu1 ion, and this facilitates the loading of hydrogen molecules onto that site with the inclusion of induced dipole interactions. The Cu1 ion has the lower charge of the two Cu^{2+} ions in crystal structure A, and this causes the Cu1 ion to interact with the hydrogen molecules less strongly. However, the Cu1 ion is still a favored site for hydrogen sorption in crystal structure A, and the hydrogen molecules do sorb there at low loading. Note, because crystal structure A has the higher charge on the Cu2 ion, this site gets loaded at higher pressures after all the Cu1 ions are filled. This can be observed in the simulated BSSP model sorption isotherms for the two unit cells at 77 K as the uptakes in crystal structure A surpass those in crystal structure B at approximately 0.80 atm.

For Eddaoudi et al.'s data, the experimental Q_{st} values for H_2 in *rht*-MOF-7 were determined by applying the virial method[83] to the experimental hydrogen sorption isotherms at 77 and 87 K. Similar numerical methods were used to calculate the Q_{st} for H_2 in the work of Li et al. The two experimental Q_{st} plots are shown in Figure 11c. The initial hydrogen Q_{st} value for Eddaoudi et al.'s data is 6.77 kJ mol^{-1}, while Li et al. calculated a value of 8.29 kJ mol^{-1}. Eddaoudi et al.'s Q_{st} values decreases to about 4.95 kJ mol^{-1} at a loading of 250 cm^3 g^{-1}. Li et al.'s Q_{st} values decline to approximately 5.80 kJ mol^{-1} at a loading of 150 cm^3 g^{-1} (no Q_{st} data is available beyond 150 cm^3 g^{-1} for Li et al.'s data). Indeed, there is a big difference in the Q_{st} values calculated by both groups, which makes sense based on their respective hydrogen sorption isotherms.

The Q_{st} values for the Buch model for both crystal structures of *rht*-MOF-7 were observed to underestimate Eddaoudi et al.'s experimental data at low loading. This is consistent with the notion that van der Waals interactions are not sufficient to capture the sorption of hydrogen onto the open-metal sites. As the loading increases, the Buch model Q_{st} values agree with Eddaoudi et al.'s data between 200 to 250 cm^3 g^{-1}. In addition, the Buch model produced similar Q_{st} values in both unit cells, which is consistent to the Buch model isotherms that were produced in these crystal structures. For the BSS model, the Q_{st} values are in good agreement with Eddaoudi et al.'s experimental data across all loadings for both crystal structures. The Q_{st} values are slightly higher in crystal structure B compared to crystal structure A, which probably signifies more H_2 molecules sorbing onto the Cu1 ions in crystal structure B.

The Q_{st} values for the BSSP model in crystal structure A are in very good agreement with Eddaoudi et al.'s Q_{st} plot. On the other hand, the Q_{st} values for the same model are higher in crystal structure B, especially at low loading. The initial Q_{st} value for the BSSP model in crystal structure B is 7.12 kJ mol^{-1}. Although this is higher than Eddaoudi et al.'s initial Q_{st}, it underestimates the initial Q_{st} value that was calculated by Li et

al. by a large amount. In crystal structure B, the Cu1 ions are binding to the hydrogen molecules more strongly due to the higher charge on this ion, which explains the increase in initial Q_{st} compared to the simulation in crystal structure A. However, as the loading increases, the BSSP model Q_{st} values in crystal structure B can be seen agreeing with Eddaoudi et al.'s data between 200 to 250 cm^{3}g^{-1}.

The radial distribution functions of hydrogen molecules about the Cu1 ions at 77 K and 0.05 atm shows distinct differences between sorbate models and crystal structures (Figure 12a). The BSSP model produced a dominant peak at
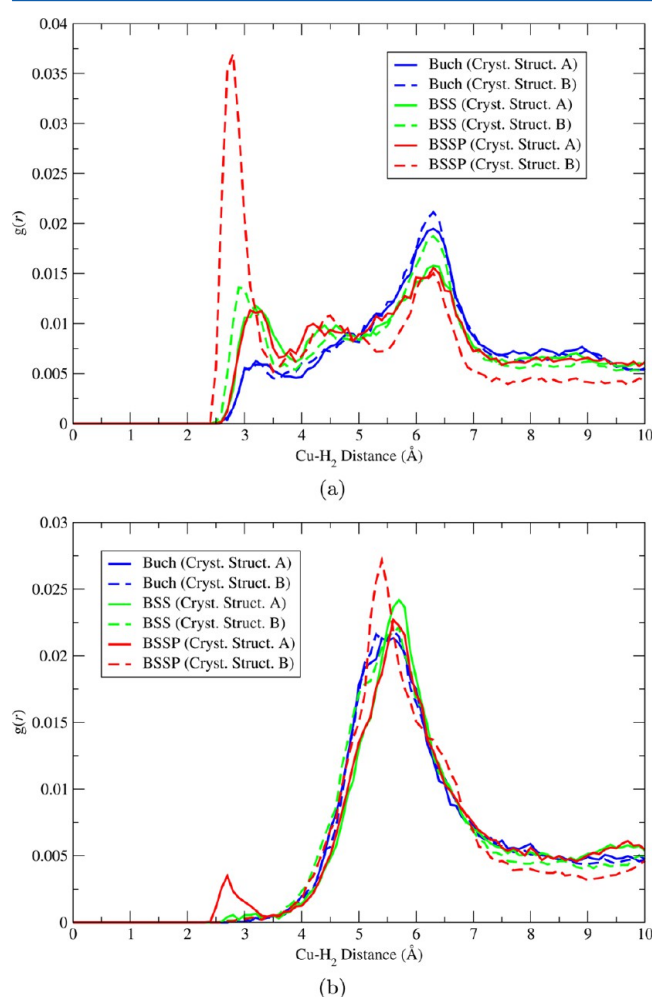

Figure 12. (a) Radial distribution function, g(r), about (a) the Cu1 ions (atom label 1 in Figure 3) and (b) the Cu2 ions (atom label 2 in Figure 3) at 77 K and 0.05 atm for the Buch model (blue), BSS model (green), and BSSP model (red). Line type indicate the unit cell in which the simulation was performed in, with solid corresponding to crystal structure A and dashed corresponding to crystal structure B.

2.8 Å in crystal structure B; this corresponds to sorption onto the Cu1 ions. While this distance is marginally greater than the Cu-D_2 distances observed in HKUST-1 via neutron powder diffraction (NPD) studies (2.39 Å)[84,85] and those found in PCN-61 and Cu-TPBTM using GCMC simulation (2.5 Å),[40,44] the proximity of the nearby Cu1 ion of another paddlewheel acts as a counter force, pulling the H_2 molecule farther away and thus making larger sorption distances possible. Examination of the system's coordinates reveal that this peak corresponds to the H_2 molecules loading between two Cu1

ions of adjacent paddlewheels in a T-shaped configuration (Figure 13a). This is consistent with the hydrogen–metal orientation seen in HKUST-1 and PCN-61/Cu-TPBTM through NPD and GCMC studies, respectively.
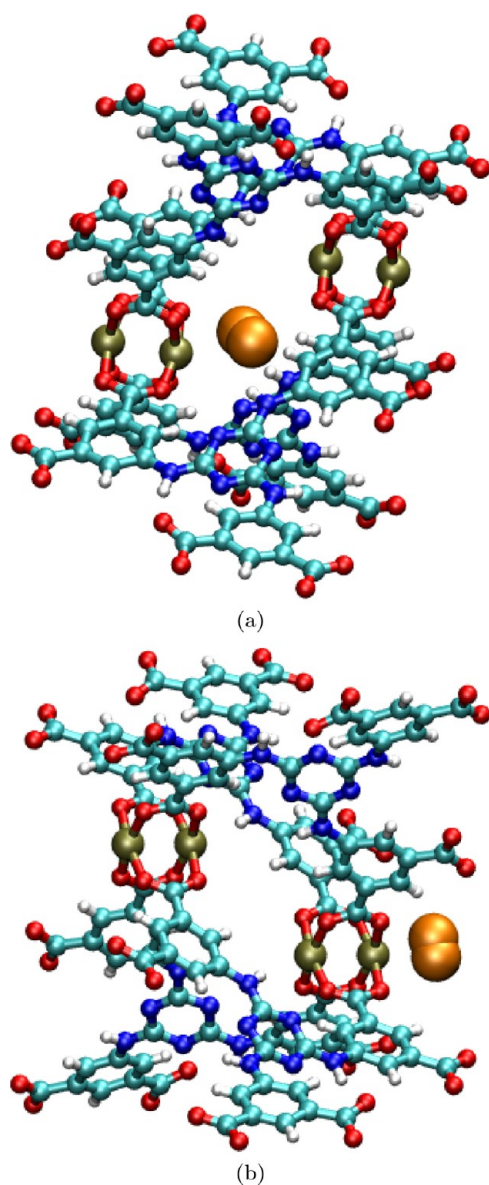

(a)

(b)

Figure 13. Molecular illustration of the BSSP H_2 molecule (orange) orientation about (a) the Cu1 ion (atom label 1 in Figure 3) and (b) the Cu2 ion (atom label 2 in Figure 3) in *rht*-MOF-7. Atom colors: C = cyan, H = white, N = blue, O = red, Cu = tan.

In crystal structure A, the peak corresponding to the sorption of BSSP H_2 molecules onto the Cu1 ion is shifted to 3.2 Å, and the magnitude of the peak is much smaller compared to that in crystal structure B as well. Since the Cu1 ion has the lower charge in crystal structure A, the hydrogen molecules cannot sorb onto this site strongly with explicit induction as a result of weaker static dipole parameters. The BSS model has a similar distribution in crystal structure A, indicating that many-body polarization effects are negligible for sorption onto the Cu1 ions in this crystal structure. In crystal structure B, the BSS and Buch models produced peaks at approximately 3.0 and 3.2 Å, respectively. Although the BSS molecules can load onto the

Cu1 ions with the correct configuration as a result of the narrow pore size for the MOF, it was observed that the loss of explicit induction reduces the nearest–neighbor peak to a third of its value. Additionally, removal of explicit electrostatics further reduces the occupancy by a factor of 2 as seen in the case for the Buch model. The radial distribution functions for the Buch model in both unit cells are very similar to each other; this is expected as differences in the charge distribution do not come into play.

The radial distribution functions of H_2 molecules about the Cu2 ions at 77 K and 0.05 atm show similar distributions for all three models in crystal structure B (Figure 12b). The peak observed at 5.3 Å for all models correspond to sorption into the corners of the truncated tetrahedral cages. This region is dominated by van der Waals interactions, and because these interactions are the major contributor to the total energy of the MOF-H_2 system, it makes sense that a large number of hydrogen molecules would sorb here. This peak is shifted to 5.5 Å in crystal structure A for all models. For the BSSP model, a small peak at 2.7 Å was found for simulations in crystal structure A. This peak corresponds to sorption onto the Cu2 ion of the metal paddlewheels. Because the Cu2 ion has the higher charge of the two Cu^{2+} ions in crystal structure A, it promotes H_2 sorption onto this site when polarization effects are included. Indeed, it can be seen through the examination of the system's coordinates that the hydrogen molecules can sorb onto the Cu2 ion in a T-shaped configuration for the BSSP model (Figure 13b). Hence, it was observed that the hydrogen molecules sorb onto both metal sites in crystal structure A. The region between the Cu1 ions is occupied first at low loading since this area is highly polarized and is dominated by electrostatics and induction, and then the Cu2 ion gets filled afterward. At higher pressures (e.g., 1.0 atm), more hydrogen molecules can sorb onto the Cu2 ions in crystal structure A and the 2.7 Å radial distribution peak that is seen for the BSSP model increases in magnitude (see Supporting Information). The Buch and BSS models cannot sorb onto this site in crystal structure A due to the lack of explicit induction terms. No such binding onto the Cu2 ions was observed in crystal structure B since the Cu2 ion has the lower charge in this structure. Note, though the hydrogen molecules are attracted to the Cu1 ions in crystal structure A despite its lower charge, this is in contrast to what was observed for CO_2 sorption in *rht*-MOF-7. For simulations of CO_2 sorption, the sorbate molecules are more sensitive to the charge on the Cu^{2+} ions of the paddlewheels, as these molecules initially sorb onto the Cu^{2+} ion that has the higher positive charge.

Examination of the normalized hydrogen dipole distribution for the BSSP model in both crystal structures at 77 K and various pressures reveals a trinodal distribution for both unit cells (Figure 14). The broad peak representing dipole magnitudes of 0.10 D and above correlates to sorption onto the open-metal sites (Figures 15a and 16a). In the case of crystal structure A, sorption is primarily observed onto the Cu2 ions, although the Cu1 ions are occupied at lower loadings. In crystal structure B, the majority of hydrogen molecules are sorbed onto the Cu1 ions. The peak from 0.070 to 0.090 D (Figure 15b) and 0.065 to 0.080 D (Figure 16b) for crystal structures A and B, respectively, corresponds to secondary sorption about the hydrogen molecules that are sorbed onto the Cu^{2+} ions of the paddleweels. Notably, in crystal structure B, the hydrogen molecules with these dipole magnitudes were also observed in the corners of the truncated tetrahedral cages
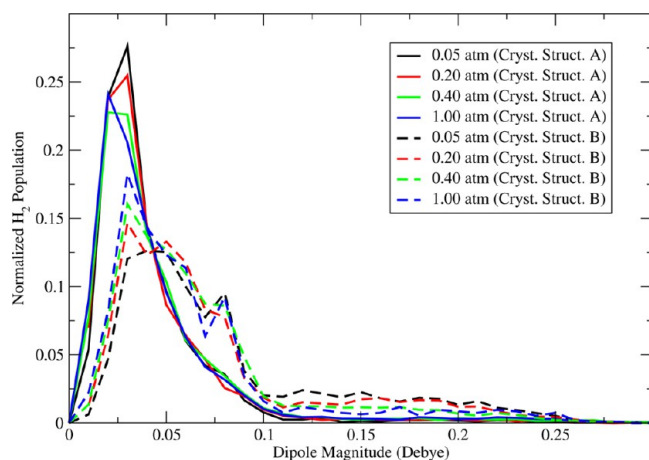
Figure 14. Normalized H_2 dipole distribution at 77 K and various pressures for the BSSP model in *rht*-MOF-7. Line type indicate the unit cell in which the simulation was performed in, with solid corresponding to crystal structure A and dashed corresponding to crystal structure B.

where the closest interaction between the hydrogen molecules and the copper paddlewheels occurs. This accounts for the greater relative population of hydrogen molecules with these dipoles in comparison to crystal structure A. The low dipole magnitude peak for both crystal structures corresponds to sorption into the truncated tetrahedral cages (Figures 15c and 16c). This includes sorption into the corners of those cages for crystal structure B and secondary sorption into that region for both crystal structures. Additionally, loading onto the center of ligand near the triazine groups was observed in both structures, though with less frequency than sorption into the corners of the truncated tetrahedral cages.

While the first and second favored binding sites for hydrogen sorption in *rht*-MOF-7 corresponds to sorption onto the Cu1 and Cu2 ions, respectively, it was determined from the simulations that the third and fourth sites in this MOF corresponds to sorption onto the center of the linkers (Figure 17a) and into the corners of the truncated tetrahedral cages (Figure 17b), respectively. In the latter case, this site consists of loading in the area between three copper paddlewheels which constitutes a cavity that can accommodate between three to four hydrogen molecules. In the case of the third binding site, loading occurs onto the 1,3,5-triazine nitrogen atoms within the same cage. While sorption onto this site from the truncated octahedral cage does occur, this is considerably less frequent due to the more spacious interior of this cage. Due to the preference for the truncated tetrahedral cages, the center of each linker in *rht*-MOF-7 can sorb up to three hydrogen molecules.

In order to confirm the theoretical predictions of the hydrogen sorption sites in *rht*-MOF-7, inelastic neutron scattering (INS) studies were performed for hydrogen in the MOF. More details of collecting the experimental INS spectra can be found in the Supporting Information. The INS spectra from hydrogen molecules sorbed in *rht*-MOF-7 are shown in Figure 18 for five different loadings. The amounts of hydrogen sorbed were calculated relative to the number of Cu^{2+} ion sites in the structure in an initial attempt to attribute the observed peaks to different binding sites, and were taken to be 0.75, 1.5, 2.25, 3, and 4 H_2 per formula unit, respectively. The highest
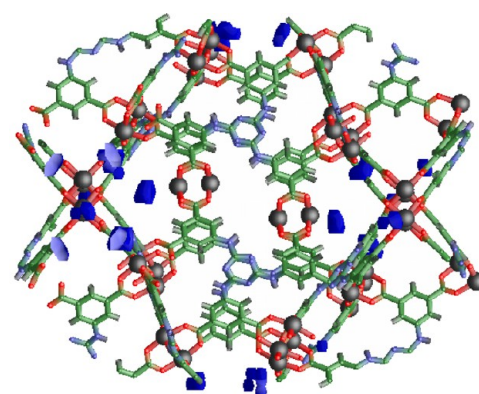
(a) 0.10 D and Above
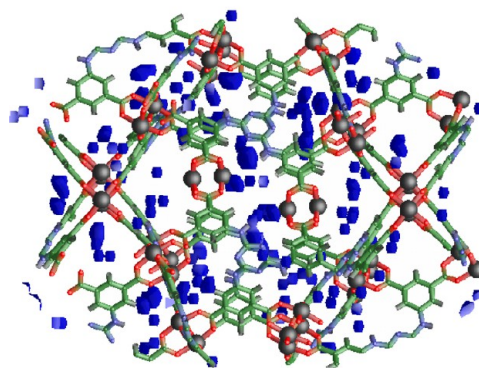
(b) 0.070 D to 0.090 D
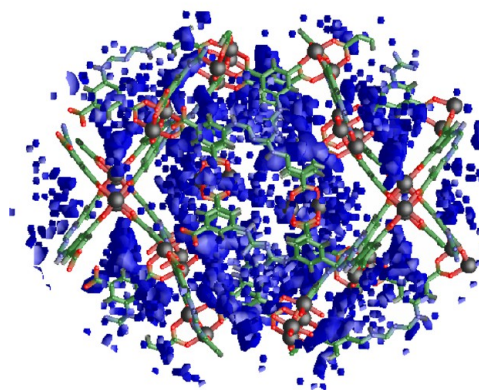
(c) 0.00 D to 0.030 D

Figure 15. 3-D histograms of H_2 sorption for the BSSP model in *rht*-MOF-7 at 77 K and 0.20 atm showing the regions of occupancy (blue) as a function of induced dipole magnitude for crystal structure A: (a) 0.10 D and above; (b) 0.070 to 0.090 D; (c) 0.00 to 0.030 D. Atom colors: C = green, H = white, N = blue, O = red, Cu = black.

loading corresponds to 14.94 mmol g^{-1} (2.92 wt %) of H_2 sorbed.

Perhaps the most noteworthy feature of the INS spectra is a peak at a relatively low energy for hydrogen in the MOF, namely, at 6.8 meV, the intensity of which appears to saturate below the second loading (1.5 H_2/formula unit). The low energy of this rotational tunneling transition is indicative of a high barrier to rotation, and hence a strong interaction with the host. This binding site must therefore be the rather unique location where the hydrogen molecule is bound between two Cu^{2+} ion sites, specifically the Cu1 ions in *rht*-MOF-7 (Figure 13a). This conclusion is convincingly supported by our calculation of the two-dimensional quantum rotational energy
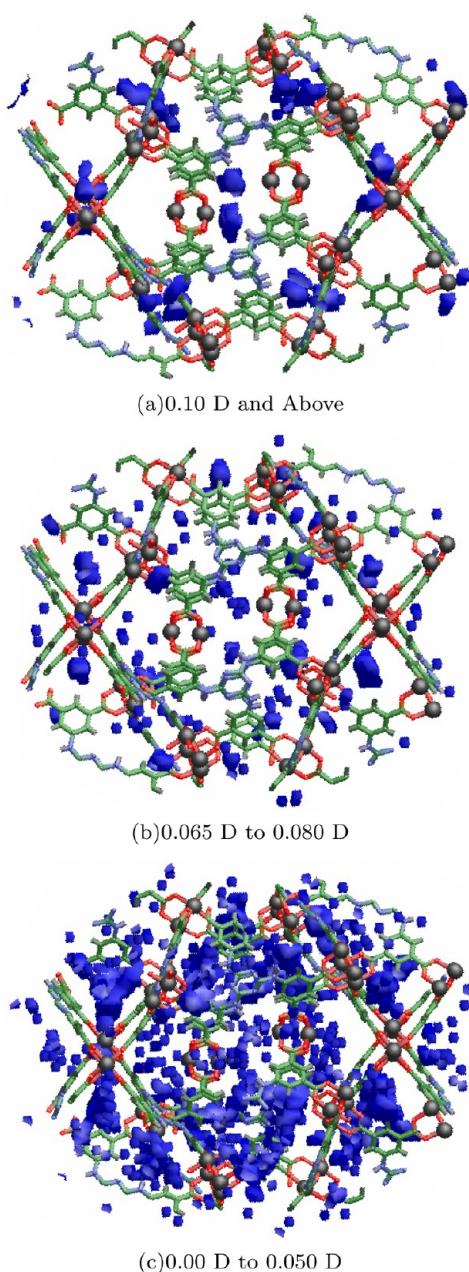
(a)0.10 D and Above

(b)0.065 D to 0.080 D

(c)0.00 D to 0.050 D

Figure 16. 3-D histograms of H$_2$ sorption for the BSSP model in *rht*-MOF-7 at 77 K and 0.20 atm showing the regions of occupancy (blue) as a function of induced dipole magnitude for crystal structure B: (a) 0.10 D and above; (b) 0.065 to 0.080 D; (c) 0.00 to 0.050 D. Atom colors: C = green, H = white, N = blue, O = red, Cu = black.

(a)

(b)

Figure 17. Molecular illustration of the BSSP H$_2$ molecule (orange) orientation about (a) the center of the linker near the triazine group and (b) the corner of the truncated tetrahedral cage in *rht*-MOF-7. Atom colors: C = cyan, H = white, N = blue, O = red, Cu = tan.

Figure 18. Inelastic neutron scattering (INS) spectra for hydrogen in *rht*-MOF-7 at different loadings: 0.75 H$_2$/formula unit (black), 1.5 H$_2$/formula unit (red), 2.25 H$_2$/formula unit (green), 3 H$_2$/formula unit (blue), and 4 H$_2$/formula unit (magenta). The calculated transitions for the different sites as shown in Table 4 are depicted as vertical colored lines: site 1 = black, site 2 = red, site 3 = green, site 4 = blue.

levels, which gives a value of 6.84 meV for H$_2$ at this site for the lowest transition (see Table 4). Note, more details of the quantum rotation calculations performed in this work is provided in the Supporting Information. The second site to be gradually populated at higher loadings has a transition at approximately 9.0 meV, which is typical for a hydrogen molecule located near a single open-metal Cu^{2+} ion site of the paddlewheel unit (as observed in HKUST-1,[84,85] PCN-12,[19] etc.), that is, the Cu2 ion site in the present system, and this again is in excellent agreement with our calculations (9.19 meV). Note that the occupancy of this site (intensity of the INS band) increases rather more slowly than the number of hydrogen molecules available after site 1 is completely filled.
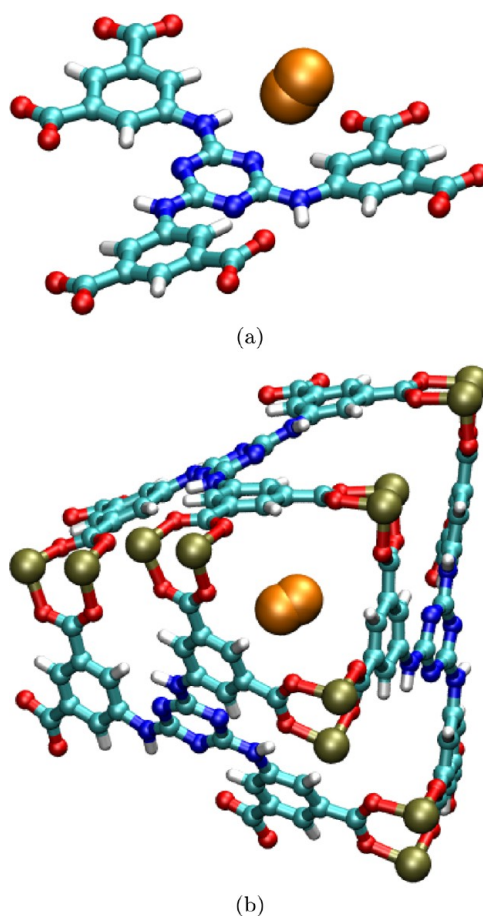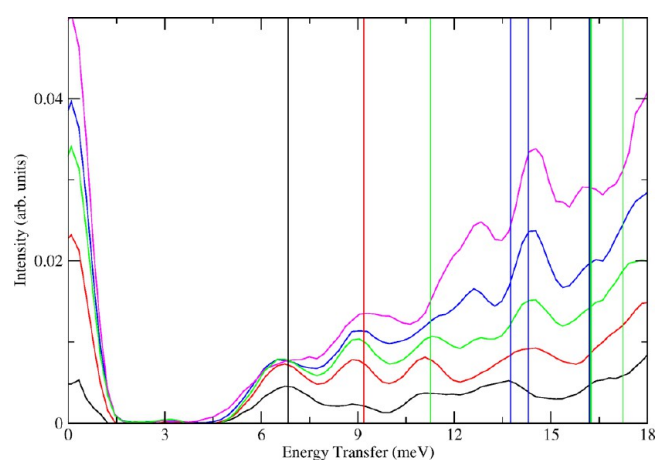
Additional peaks at approximately 11.0 and 13.5 meV are apparent in the INS spectra even at low loadings, and these must arise from hydrogen molecules sorbing to different binding sites. It would be difficult to identify these sites without

Table 4. Calculated Two-Dimensional Quantum Rotational Levels (in meV) for a Hydrogen Molecule at Different Sites in *rht*-MOF-7[a]

n	j	site 1 ΔE (meV)	site 2 ΔE (meV)	site 3 ΔE (meV)	site 4 ΔE (meV)
1	0	0.00	0.00	0.00	0.00
2		6.84	9.19	11.26	13.74
3	1	16.19	21.55	16.25	14.30
4		29.23	26.30	17.24	16.21
5		37.31	40.49	42.13	43.09
6		41.83	50.66	42.84	43.12
7	2	46.65	54.48	43.55	44.46
8		54.64	62.02	46.96	44.88
9		62.88	74.62	47.05	45.31

[a]Sites 1, 2, 3, and 4 are depicted in Figures 13a, 13b, 17a, and 17b, respectively. The energies are given relative to E_0, which are −68.05, −68.40, −57.35, and −76.67 meV for the respective sites.

our computational work, which does, however, give clear indications as to their nature. The center of each linker in *rht*-MOF-7 can sorb up to three hydrogen molecules, with each hydrogen molecule coordinating to a triazine nitrogen atom (Figure 17a), and these give rise to the peak at around 11.0 meV (site 3), or 11.26 meV in our calculation. Finally, the peak observed in the INS spectra at about 13.5 meV (site 4), can be associated with the hydrogen molecules that can sorb into the corners of the truncated tetrahedral cages (Figure 17b), for which we calculate rotational transitions of 13.74 and 14.30 meV for the two lowest transitions. It should be noted that the peaks corresponding to sites 3 and 4 in the INS spectra exhibit significant shifts toward higher frequencies as the loading of hydrogen is increased. This observation can be rationalized by assuming that some of the weakly sorbed hydrogen molecules are forced farther away from the framework when the space becomes more crowded at higher loadings. This would lower the respective barriers to rotation, and hence increase the rotational frequencies. The excellent agreement between our calculated and observed rotational transitions for all four hydrogen binding sites extends to some of the higher transitions, as the peaks in the INS spectra at approximately 16.0 and 18.0 meV correspond quite well to the second or third transitions for some of the sites (see Table 4).

IV. CONCLUSION

In conclusion, simulations of CO_2 and H_2 sorption in *rht*-MOF-7 were performed to better understand the sorption mechanism in this material. It was shown that the simulated CO_2 sorption isotherms and Q_{st} values were in better agreement with the measurements reported by Eddaoudi et al. in both crystal structures for the polarizable CO_2 potential used herein. In addition, it was observed that simulations involving the inclusion of explicit polarization caused a favorable ordering of the CO_2 molecules inside the MOF, which decreased overall sorption into agreement with Eddaoudi et al.'s experimental data at lower temperatures. It was discovered through the modeling studies that a favorable interaction between the CO_2 molecules and the Cu1 ions of neighboring paddlewheels is responsible for the MOF's high CO_2 uptake and initial Q_{st}. Simulations using the well-known TraPPE model showed significant oversorption of Eddaoudi et al.'s experimental results, but interestingly displayed rough agreement to Li et al.'s isotherm at all temperatures considered. However,

inspection of the modeled structure revealed that the TraPPE CO_2 molecules were simply sorbing to regions that are dominated by van der Waals and electrostatic interactions and were weakly sorbing to regions dominated by induction (e.g., the open-metal sites).

Furthermore, the simulated low pressure H_2 sorption isotherms and Q_{st} values were also in good agreement to Eddaoudi et al.'s experimental data. Many-body polarization interactions were negligible for hydrogen uptake in *rht*-MOF-7, which was attributed to the narrow pore sizes that are displayed by the MOF. The small pore sizes caused short-range dispersion to dominate, while polarization effects cancel somewhat in the high symmetry environment. However, many-body polarization effects were important at initial loadings for sorption onto the open-metal sites. This was confirmed by examining the radial distribution functions about both Cu^{2+} ions for all models in both crystal structures. Indeed, notable deviations in the sorption sites were observed when this energetic contribution was neglected, especially about the open-metal sites.

The slight differences in the atomic positions in both reported crystallographic structures of *rht*-MOF-7 resulted in different electrostatic parameters about the Cu^{2+} ions of the metal paddlewheels. As a result, the gas sorption mechanisms in the respective unit cells were different at low loading, although, this did not significantly change the overall sorption capacity in *rht*-MOF-7. In one structure (crystal structure B), the most favorable CO_2 sorption site was observed as the molecules coordinated between two Cu^{2+} ions of adjacent paddlewheels that face toward the center of the linker (Cu1 ions). In the other structure (crystal structure A), the initial sorption site was the other chemically distinct Cu^{2+} ion (Cu2 ion) with an initial Q_{st} value that is inconsistent with the experimental value. Furthermore, the high experimental initial Q_{st} value for CO_2 in *rht*-MOF-7 could only be produced in crystal structure B with the inclusion of many-body polarization. Sorption between two Cu1 ions of adjacent paddlewheels was the most energetically favorable site for CO_2 sorption in the MOF, and this site was strongly captured in simulation if the Cu1 ions have the higher partial positive charge relative to the Cu2 ions.

The INS spectra for hydrogen in *rht*-MOF-7 revealed four noticeable transitions, with each transition corresponding to a specific binding site in the MOF. The polarization distribution served as an order parameter to identify the different hydrogen sorption sites in this MOF. Four distinct sites were identified for hydrogen sorption in *rht*-MOF-7 in this work: (1) between two Cu1 ions of adjacent paddlewheels; (2) the Cu2 ions; (3) the center of the linker near the triazine nitrogen atoms; and (4) the corners of the truncated tetrahedral cages. Calculation of the two-dimensional quantum rotational levels for a hydrogen molecule about each site considered in the MOF revealed a j = 0 to 1 transition that matched a certain peak in the INS spectra. Hence, there was a very good agreement between the transitions observed in the INS spectra and the calculated rotational transitions for each site. Additionally, according to the INS spectra, the region between the Cu1 ions is highly favored at low loadings, while the Cu2 ions become occupied at higher loadings. This result is consistent to what was observed in the simulations for hydrogen sorption, especially for simulation in crystal structure A.

In sum, while it is difficult to ascertain exactly what is happening experimentally concerning differing sorption by the two experimental groups, these results demonstrate the

effectiveness of good theoretical models in identifying salient physical sorption interactions and their sensitivity to small but significant physical modifications. The GCMC results at minimum clarify the general processes involved in CO_2 and H_2 sorption in this material. The kinds of insights that can be gained highlight the power of theory and experiment used together as part of an interpretive and design process.

Future work includes simulating sorption of other sorbates such as N_2, CH_4, and H_2O in *rht*-MOF-7 and insightfully comparing results to experimental data. This will be performed using accurate and transferable potentials of these sorbates that have been developed in our group.[80,86] In addition, performing simulation of multicomponent mixtures will be a task that will be investigated using these potentials. The selectivities that are obtained from GCMC simulation will be compared to those measured experimentally via ideal adsorbed solution theory (IAST)[87] calculations and column breakthrough experiments. Examination of the sorption mechanisms in other *rht*-MOFs is currently ongoing.

ASSOCIATED CONTENT

Supporting Information

Details of the electronic structure calculations, simulation methods, quantum rotation calculations, and experimental INS studies, many-body polarization overview, tables of properties, pictures of MOF fragments, and additional content. This material is available free of charge via the Internet at http://pubs.acs.org.

AUTHOR INFORMATION

Corresponding Author
*E-mail: brian.b.space@gmail.com.

Author Contributions
‡These authors contributed equally (T.P. and K.A.F.).

Notes
The authors declare no competing financial interest.

ACKNOWLEDGMENTS

REFERENCES

(1) Annual Energy Output. 2012; http://www.eia.gov/forecasts/aeo/.

(2) International Energy Output. 2011. http://www.eia.gov/forecasts/ieo/index.cfm.

(3) Carbon dioxide passes symbolic mark. 2013; http://www.bbc.co.uk/news/science-environment-22486153, accessed June 26, 2013.

(4) Herzog, H.; Drake, E.; Adams, E. CO_2 capture, reuse, and storage technologies for mitigating global climate change. 1997; http://sequestration.mit.edu/pdf/WhitePaper.pdf.

(5) Figueroa, J. D.; Fout, T.; Plasynski, S.; McIlvried, H.; Srivastava, R. D. Advances in CO_2 capture technology—The U.S. Department of Energy's Carbon Sequestration Program. *Int. J. Greenhouse Gas Control* **2008**, *2*, 9−20.

(6) Schlapbach, L.; Zuttel, A. Hydrogen-storage materials for mobile applications. *Nature* **2001**, *414*, 353−358.

(7) Klontzas, E.; Mavrandonakis, A.; Tylianakis, E.; Froudakis, G. E. Improving hydrogen storage capacity of MOF by functionalization of the organic linker with lithium atoms. *Nano Lett.* **2008**, *8*, 1572−1576.

(8) DOE Targets for onboard hydrogen storage systems for light-duty vehicles. 2009; http://www1.eere.energy.gov/hydrogenandfuelcells/storage/pdfs/targets_onboard_hydro_storage.pdf.

(9) Yang, Q.; Zhong, C.; Chen, J.-F. Computational study of CO_2 storage in metal−organic frameworks. *J. Phys. Chem. C* **2008**, *112*, 1562−1569.

(10) Sumida, K.; Rogow, D. L.; Mason, J. A.; McDonald, T. M.; Bloch, E. D.; Herm, Z. R.; Bae, T.-H.; Long, J. R. Carbon dioxide capture in metal−organic frameworks. *Chem. Rev.* **2012**, *112*, 724−781.

(11) Nugent, P.; Belmabkhout, Y.; Burd, S. D.; Cairns, A. J.; Luebke, R.; Forrest, K.; Pham, T.; Ma, S.; Space, B.; Wojtas, L.; Eddaoudi, M.; Zaworotko, M. J. Porous materials with optimal adsorption thermodynamics and kinetics for CO_2 separations. *Nature* **2013**, *495*, 80−84.

(12) Collins, D. J.; Ma, S.; Zhou, H.-C. In *Metal−Organic Frameworks: Design and Application*; MacGillivray, L. R., Ed.; John Wiley & Sons, Inc.: Hoboken, NJ, 2010; pp 249−266.

(13) Collins, D. J.; Zhou, H.-C. Hydrogen storage in metal−organic frameworks. *J. Mater. Chem.* **2007**, *17*, 3154−3160.

(14) Suh, M. P.; Park, H. J.; Prasad, T. K.; Lim, D.-W. Hydrogen storage in metal−organic frameworks. *Chem. Rev.* **2012**, *112*, 782−835.

(15) Yaghi, O. M.; Li, H.; Davis, C.; Richardson, D.; Groy, T. L. Synthetic strategies, structure patterns, and emerging properties in the chemistry of modular porous solids. *Acc. Chem. Res.* **1998**, *31*, 474−484.

(16) Eddaoudi, M.; Moler, D. B.; Li, H.; Chen, B.; Reineke, T. M.; O'Keeffe, M.; Yaghi, O. M. Modular chemistry: Secondary building units as a basis for the design of highly porous and robust metal−organic carboxylate frameworks. *Acc. Chem. Res.* **2001**, *34*, 319−330.

(17) Farha, O. K.; Yazaydin, A. Ö.; Eryazici, I.; Malliakas, C. D.; Hauser, B. G.; Kanatzidis, M. G.; Nguyen, S. T.; Snurr, R. Q.; Hupp, J. T. De novo synthesis of a metal−organic framework material featuring ultrahigh surface area and gas storage capacities. *Nat. Chem.* **2010**, *2*, 944−948.

(18) Eddaoudi, M.; Eubank, J. F. In *Metal-Organic Frameworks: Design and Application*; MacGillivray, L. R., Ed.; John Wiley & Sons, Inc.: Hoboken, NJ, 2010; pp 37−89.

(19) Wang, X.-S.; Ma, S.; Forster, P.; Yuan, D.; Eckert, J.; López, J.; Murphy, B.; Parise, J.; Zhou, H.-C. Enhancing H_2 uptake by "close-packing" alignment of open copper sites in metal−organic frameworks. *Angew. Chem., Int. Ed.* **2008**, *47*, 7263−7266.

(20) Nouar, F.; Eubank, J. F.; Bousquet, T.; Wojtas, L.; Zaworotko, M. J.; Eddaoudi, M. Supermolecular building blocks (SBBs) for the design and synthesis of highly porous metal−organic frameworks. *J. Am. Chem. Soc.* **2008**, *130*, 1833−1835.

(21) Zou, Y.; Park, M.; Hong, S.; Lah, M. S. A designed metal-organic framework based on a metal-organic polyhedron. *Chem. Commun.* **2008**, 2340−2342.

(22) Zhao, D.; Yuan, D.; Sun, D.; Zhou, H.-C. Stabilization of metal−organic frameworks with high surface areas by the incorporation of mesocavities with microwindows. *J. Am. Chem. Soc.* **2009**, *131*, 9186−9188.

(23) Yuan, D.; Zhao, D.; Sun, D.; Zhou, H.-C. An isoreticular series of metal−organic frameworks with dendritic hexacarboxylate ligands

and exceptionally high gas-uptake capacity. *Angew. Chem. Int. Ed.* **2010**, *122*, 5485−5489.

(24) Zheng, B.; Bai, J.; Duan, J.; Wojtas, L.; Zaworotko, M. J. Enhanced CO_2 binding affinity of a high-uptake rht-type metal−organic framework decorated with acylamide groups. *J. Am. Chem. Soc.* **2011**, *133*, 748−751.

(25) Yan, Y.; Yang, S.; Blake, A. J.; Lewis, W.; Poirier, E.; Barnett, S. A.; Champness, N. R.; Schröder, M. A mesoporous metal−organic framework constructed from a nanosized C_3-symmetric linker and $[Cu_{24}(isophthalate)_{24}]$ cuboctahedra. *Chem. Commun.* **2011**, *47*, 9995−9997.

(26) Li, B.; et al. Enhanced binding affinity, remarkable selectivity, and high capacity of CO_2 by dual functionalization of a rht-type metal−organic framework. *Angew. Chem., Int. Ed.* **2012**, *51*, 1412−1415.

(27) Eryazici, I.; Farha, O. K.; Hauser, B. G.; Yazaydin, A. Ö.; Sarjeant, A. A.; Nguyen, S. T.; Hupp, J. T. Two large-pore metal−organic frameworks derived from a single polytopic strut. *Cryst. Growth Des.* **2012**, *12*, 1075−1080.

(28) Zheng, B.; Yang, Z.; Bai, J.; Li, Y.; Li, S. High and selective CO_2 capture by two mesoporous acylamide-functionalized rht-type metal-organic frameworks. *Chem. Commun.* **2012**, *48*, 7025−7027.

(29) Luebke, R.; Eubank, J. F.; Cairns, A. J.; Belmabkhout, Y.; Wojtas, L.; Eddaoudi, M. The unique rht-MOF platform, ideal for pinpointing the functionalization and CO_2 adsorption relationship. *Chem. Commun.* **2012**, *48*, 1455−1457.

(30) Eubank, J. F.; Nouar, F.; Luebke, R.; Cairns, A. J.; Wojtas, L.; Alkordi, M.; Bousquet, T.; Hight, M. R.; Eckert, J.; Embs, J. P.; Georgiev, P. A.; Eddaoudi, M. On demand: The singular rht Net, an ideal blueprint for the construction of a metal−organic framework (MOF) platform. *Angew. Chem., Int. Ed.* **2012**, *51*, 10099−10103.

(31) Farha, O. K.; Wilmer, C. E.; Eryazici, I.; Hauser, B. G.; Parilla, P. A.; O'Neill, K.; Sarjeant, A. A.; Nguyen, S. T.; Snurr, R. Q.; Hupp, J. T. Designing higher surface area metal−organic frameworks: Are triple bonds better than phenyls? *J. Am. Chem. Soc.* **2012**, *134*, 9860−9863.

(32) Farha, O. K.; Eryazici, I.; Jeong, N. C.; Hauser, B. G.; Wilmer, C. E.; Sarjeant, A. A.; Snurr, R. Q.; Nguyen, S. T.; Yazaydin, A. Ö.; Hupp, J. T. Metal−organic framework materials with ultrahigh surface areas: Is the sky the limit? *J. Am. Chem. Soc.* **2012**, *134*, 15016−15021.

(33) Zhao, X.; Sun, D.; Yuan, S.; Feng, S.; Cao, R.; Yuan, D.; Wang, S.; Dou, J.; Sun, D. Comparison of the effect of functional groups on gas-uptake capacities by fixing the volumes of cages A and B and modifying the inner wall of cage C in rht-type MOFs. *Inorg. Chem.* **2012**, *51*, 10350−10355.

(34) Wang, X.-J.; Li, P.-Z.; Chen, Y.; Zhang, Q.; Zhang, H.; Chan, X. X.; Ganguly, R.; Li, Y.; Jiang, J.; Zhao, Y. A rationally designed nitrogen-rich metal-organic framework and its exceptionally high CO_2 and H_2 uptake capability. *Sci. Rep.* **2013**, *3*, DOI: 10.1038/srep01149.

(35) Wilmer, C. E.; Farha, O. K.; Yildirim, T.; Eryazici, I.; Krungleviciute, V.; Sarjeant, A. A.; Snurr, R. Q.; Hupp, J. T. Gram-scale, high-yield synthesis of a robust metal−organic framework for storing methane and other gases. *Energy Environ. Sci.* **2013**, *6*, 1158−1163.

(36) Yan, Y.; Suyetin, M.; Bichoutskaia, E.; Blake, A. J.; Allan, D. R.; Barnett, S. A.; Schröder, M. Modulating the packing of $[Cu_{24}(isophthalate)_{24}]$ cuboctahedra in a triazole-containing metal−organic polyhedral framework. *Chem. Sci.* **2013**, *4*, 1731−1736.

(37) Wu, H.; Yao, K.; Zhu, Y.; Li, B.; Shi, Z.; Krishna, R.; Li, J. Cu-TDPAT, an rht-type dual-functional metal−organic framework offering significant potential for use in H_2 and natural gas purification processes operating at high pressures. *J. Phys. Chem. C* **2012**, *116*, 16609−16618.

(38) Belof, J. L.; Stern, A. C.; Eddaoudi, M.; Space, B. On the mechanism of hydrogen storage in a metal−organic framework material. *J. Am. Chem. Soc.* **2007**, *129*, 15202−15210.

(39) Snurr, R. Q.; Yazaydin, A. Ö.; Dubbeldam, D.; Frost, H. In *Metal-Organic Frameworks: Design and Application*; MacGillivray, L. R., Ed.; John Wiley & Sons, Inc.: Hoboken, NJ, 2010; pp 313−339.

(40) Forrest, K. A.; Pham, T.; McLaughlin, K.; Belof, J. L.; Stern, A. C.; Zaworotko, M. J.; Space, B. Simulation of the mechanism of gas sorption in a metal−organic framework with open metal sites: Molecular hydrogen in PCN-61. *J. Phys. Chem. C* **2012**, *116*, 15538−15549.

(41) Applequist, J.; Carl, J. R.; Fung, K.-K. Atom dipole interaction model for molecular polarizability. Application to polyatomic molecules and determination of atom polarizabilities. *J. Am. Chem. Soc.* **1972**, *94*, 2952−2960.

(42) Thole, B. Molecular polarizabilities calculated with a modified dipole interaction. *Chem. Phys.* **1981**, *59*, 341−350.

(43) van Duijnen, P. T.; Swart, M. Molecular and atomic polarizabilities: Thole's model revisited. *J. Phys. Chem. A* **1998**, *102*, 2399−2407.

(44) Pham, T.; Forrest, K. A.; Nugent, P.; Belmabkhout, Y.; Luebke, R.; Eddaoudi, M.; Zaworotko, M. J.; Space, B. Understanding hydrogen sorption in a metal−organic framework with open-metal sites and amide functional groups. *J. Phys. Chem. C* **2013**, *117*, 9340−9354.

(45) Mankoo, P. K.; Keyes, T. Classical molecular electrostatics: Recognition of ligands in proteins and the vibrational stark effect. *J. Phys. Chem. B* **2006**, *110*, 25074−25079.

(46) Keyes, T.; Napoleon, R. L. Extending classical molecular theory with polarization. *J. Phys. Chem. B* **2011**, *115*, 522−531.

(47) Fang, H.; Demir, H.; Kamakoti, P.; Sholl, D. Recent developments in first-principles force fields for molecules in nanoporous materials. *J. Mater. Chem. A* **2014**, *2*, 274−291.

(48) Belof, J. L.; Stern, A. C.; Space, B. An accurate and transferable intermolecular diatomic hydrogen potential for condensed phase simulation. *J. Chem. Theory Comput.* **2008**, *4*, 1332−1337.

(49) Zhang, Z.; Li, Z.; Li, J. Computational study of adsorption and separation of CO_2, CH_4, and N_2 by an rht-type metal−organic framework. *Langmuir* **2012**, *28*, 12122−12133.

(50) Walton, K. S.; Millward, A. R.; Dubbeldam, D.; Frost, H.; Low, J. J.; Yaghi, O. M.; Snurr, R. Q. Understanding inflections and steps in carbon dioxide adsorption isotherms in metal−organic frameworks. *J. Am. Chem. Soc.* **2008**, *130*, 406−407.

(51) Martin, M. G.; Siepmann, J. I. Transferable potentials for phase equilibria. 1. United-atom description of *n*-alkanes. *J. Phys. Chem. B* **1998**, *102*, 2569−2577.

(52) Potoff, J. J.; Siepmann, J. I. Vapor−liquid equilibria of mixtures containing alkanes, carbon dioxide, and nitrogen. *AIChE J.* **2001**, *47*, 1676−1682.

(53) Mullen, A. L.; Pham, T.; Forrest, K. A.; Cioce, C. R.; McLaughlin, K.; Space, B. A polarizable and transferable PHAST CO_2 potential for materials simulation. *J. Chem. Theory Comput.* **2013**, *9*, 5421−5429.

(54) Rappé, A. K.; Casewit, C. J.; Colwell, K. S.; Goddard, W. A.; Skiff, W. M. UFF, a full periodic table force field for molecular mechanics and molecular dynamics simulations. *J. Am. Chem. Soc.* **1992**, *114*, 10024−10035.

(55) Stern, A. C.; Belof, J. L.; Eddaoudi, M.; Space, B. Understanding hydrogen sorption in a polar metal−organic framework with constricted channels. *J. Chem. Phys.* **2012**, *136*, 034705.

(56) Pham, T.; Forrest, K. A.; McLaughlin, K.; Tudor, B.; Nugent, P.; Hogan, A.; Mullen, A.; Cioce, C. R.; Zaworotko, M. J.; Space, B. Theoretical investigations of CO_2 and H_2 sorption in an inter-penetrated square-pillared metal−organic material. *J. Phys. Chem. C* **2013**, *117*, 9970−9982.

(57) Forrest, K. A.; Pham, T.; Hogan, A.; McLaughlin, K.; Tudor, B.; Nugent, P.; Burd, S. D.; Mullen, A.; Cioce, C. R.; Wojtas, L.; Zaworotko, M. J.; Space, B. Computational studies of CO_2 sorption and separation in an ultramicroporous metal−organic material. *J. Phys. Chem. C* **2013**, *117*, 17687−17698.

(58) Forrest, K. A.; Pham, T.; Nugent, P.; Burd, S. D.; Mullen, A.; Wojtas, L.; Zaworotko, M. J.; Space, B. Examining the effects of different ring configurations and equatorial fluorine atom positions on CO_2 sorption in $[Cu(bpy)_2SiF_6]$. *Cryst. Growth Des.* **2013**, *13*, 4542−4548.

(59) Pham, T.; Forrest, K. A.; Hogan, A.; McLaughlin, K.; Belof, J. L.; Eckert, J.; Space, B. Simulations of hydrogen sorption in *rht*-MOF-1: Identifying the binding sites through explicit polarization and quantum rotation calculations. *J. Mater. Chem. A* **2014**, DOI: 10.1039/C3TA14591C.

(60) Kresse, G.; Hafner, J. Ab initio molecular dynamics for liquid metals. *Phys. Rev. B* **1993**, *47*, 558−561.

(61) Kresse, G.; Hafner, J. Ab initio molecular-dynamics simulation of the liquid-metal−amorphous-semiconductor transition in germanium. *Phys. Rev. B* **1994**, *49*, 14251−14269.

(62) Kresse, G.; Furthmüller, J. Efficiency of ab initio total energy calculations for metals and semiconductors using a plane-wave basis set. *Comput. Mater. Sci.* **1996**, *6*, 15−50.

(63) Kresse, G.; Furthmüller, J. Efficient iterative schemes for ab initio total-energy calculations using a plane-wave basis set. *Phys. Rev. B* **1996**, *54*, 11169−11186.

(64) Chen, D.-L.; Stern, A. C.; Space, B.; Johnson, J. K. Atomic charges derived from electrostatic potentials for molecular and periodic systems. *J. Phys. Chem. A* **2010**, *114*, 10225−10233.

(65) Watanabe, T.; Manz, T. A.; Sholl, D. S. Accurate treatment of electrostatics during molecular adsorption in nanoporous crystals without assigning point charges to framework atoms. *J. Phys. Chem. C* **2011**, *115*, 4824−4836.

(66) Babarao, R.; Eddaoudi, M.; Jiang, J. W. Highly porous ionic rht metal−organic framework for H_2 and CO_2 storage and separation: A molecular simulation study. *Langmuir* **2010**, *26*, 11196−11203.

(67) Cornell, W. D.; Cieplak, P.; Bayly, C. I.; Gould, I. R.; Merz, K. M.; Ferguson, D. M.; Spellmeyer, D. C.; Fox, T.; Caldwell, J. W.; Kollman, P. A. A second generation force field for the simulation of proteins, nucleic acids, and organic molecules. *J. Am. Chem. Soc.* **1995**, *117*, 5179−5197.

(68) Stevens, W. J.; Basch, H.; Krauss, M. Compact effective potentials and efficient shared exponent basis sets for the first and secondrow atoms. *J. Chem. Phys.* **1984**, *81*, 6026.

(69) Hay, P. J.; Wadt, W. R. Ab initio effective core potentials for molecular calculations. Potentials for the transition metal atoms Sc to Hg. *J. Chem. Phys.* **1985**, *82*, 270.

(70) LaJohn, L. A.; Christiansen, P. A.; Ross, R. B.; Atashroo, T.; Ermler, W. C. Ab initio relativistic effective potentials with spin−orbit operators. III. Rb through Xe. *J. Chem. Phys.* **1987**, *87*, 2812.

(71) Valiev, M.; Bylaska, E.; Govind, N.; Kowalski, K.; Straatsma, T.; Dam, H. V.; Wang, D.; Nieplocha, J.; Apra, E.; Windus, T.; de Jong, W. NWChem: A comprehensive and scalable open-source solution for large scale molecular simulations. *Comput. Phys. Commun.* **2010**, *181*, 1477−1489.

(72) Chirlian, L. E.; Francl, M. M. Atomic charges derived from electrostatic potentials: A detailed study. *J. Comput. Chem.* **1987**, *8*, 894−905.

(73) Breneman, C. M.; Wiberg, K. B. Determining atom-centered monopoles from molecular electrostatic potentials. The need for high sampling density in formamide conformational analysis. *J. Comput. Chem.* **1990**, *11*, 361−373.

(74) Bode, K. A.; Applequist, J. A new optimization of atom polarizabilities in halomethanes, aldehydes, ketones, and amides by way of the atom dipole interaction model. *J. Phys. Chem.* **1996**, *100*, 17820−17824.

(75) DeVane, R.; Space, B.; Perry, A.; Neipert, C.; Ridley, C.; Keyes, T. A time correlation function theory of two-dimensional infrared spectroscopy with applications to liquid water. *J. Chem. Phys.* **2004**, *121*, 3688−3701.

(76) Perry, A.; Neipert, C.; Space, B.; Moore, P. B. Theoretical modeling of interface specific vibrational spectroscopy: Methods and applications to aqueous interfaces. *Chem. Rev.* **2006**, *106*, 1234−1258.

(77) Cirera, J.; Sung, J. C.; Howland, P. B.; Paesani, F. The effects of electronic polarization on water adsorption in metal−organic frameworks: H_2O in MIL-53(Cr). *J. Chem. Phys.* **2012**, *137*, 054704.

(78) Paesani, F. Water in metal-organic frameworks: structure and diffusion of H_2O in MIL-53(Cr) from quantum simulations. *Mol. Simul.* **2012**, *38*, 63641.

(79) Buch, V. Path integral simulations of mixed *para*-D_2 and *ortho*-D_2 clusters: The orientational effects. *J. Chem. Phys.* **1994**, *100*, 7610−7629.

(80) McLaughlin, K.; Cioce, C. R.; Belof, J. L.; Space, B. A molecular H_2 potential for heterogeneous simulations including polarization and many-body van der Waals interactions. *J. Chem. Phys.* **2012**, *136*, 194302.

(81) Belof, J. L.; Stern, A. C.; Space, B. A predictive model of hydrogen sorption for metal−organic materials. *J. Phys. Chem. C* **2009**, *113*, 9316−9320.

(82) Wu, H.; Simmons, J. M.; Srinivas, G.; Zhou, W.; Yildirim, T. Adsorption sites and binding nature of CO_2 in prototypical metal−organic frameworks: A combined neutron diffraction and first-principles study. *J. Phys. Chem. Lett.* **2010**, *1*, 1946−1951.

(83) Dincă, M.; Dailly, A.; Liu, Y.; Brown, C. M.; Neumann, D. A.; Long, J. R. Hydrogen storage in a microporous metal−organic framework with exposed Mn^{2+} coordination sites. *J. Am. Chem. Soc.* **2006**, *128*, 16876−16883.

(84) Peterson, V. K.; Liu, Y.; Brown, C. M.; Kepert, C. J. Neutron powder diffraction study of D_2 sorption in Cu_3(1,3,5-benzenetricarboxylate)$_2$. *J. Am. Chem. Soc.* **2006**, *128*, 15578−15579.

(85) Brown, C. M.; Liu, Y.; Yildirim, T.; Peterson, V. K.; Kepert, C. J. Hydrogen adsorption in HKUST-1: A combined inelastic neutron scattering and first-principles study. *Nanotechnology* **2009**, *20*, 204025.

(86) Cioce, C. R.; McLaughlin, K.; Belof, J. L.; Space, B. A Polarizable and transferable PHAST N_2 potential for use in materials simulation. *J. Chem. Theory Comput.* **2013**, *9*, 5550−5557.

(87) Myers, A. L.; Prausnitz, J. M. Thermodynamics of mixed-gas adsorption. *AIChE J.* **1965**, *11*, 121−127.